

## ABSTRACT

Title of Thesis: A SEMIANALYTICAL, THREE DIMENSIONAL  
MODEL OF MICROSTRUCTURE IN  
MULTIPARTICLE, MULTIPHASE FLOW

Jesse T Wimert, Master of Science, 2011

Thesis directed by: Professor Saswata Hier-Majumder  
Department of Geology

This thesis presents a three dimensional microgeodynamic model of grain-melt geometry in partially molten rocks. The isotropic unit cell of the partially molten rock is characterized by a face-centered-cubic symmetry, consisting of rhombic dodecahedral grains. The variation of surface tension between grain-grain and grain-melt contacts excites a coupled viscous flow within grains and the interstitial melt leading to a steady-state grain-melt geometry. The fractional area of intergranular contact, contiguity, is obtained from these models as a function of melt volume fraction, for melt fractions between 0.05 and 0.25. Comparison with previous results indicates that the contiguity in three dimensional models is lower than two dimensional models. We apply our model to the UltraLow Velocity Zones (ULVZ) in the Earth's core-mantle boundary. The observed seismic signature of the ULVZ can be explained by a melt volume fraction between 0.08 and 0.12.

A SEMIANALYTICAL, THREE DIMENSIONAL MODEL OF  
MICROSTRUCTURE IN MULTIPARTICLE, MULTIPHASE FLOW

by

Jesse T Wimert

Thesis submitted to the Faculty of the Graduate School of the  
University of Maryland, College Park in partial fulfillment  
of the requirements for the degree of  
Master of Science  
2011

Advisory Committee:

Professor Saswata Hier-Majumder, Chair  
Professor Sarah Penniston-Dorland  
Professor Wenlu Zhu

© Copyright by

Jesse T Wimert

2011

## Acknowledgments

This research would not have been possible without the support of many people. Foremost, I would like to express my gratitude to my advisor Prof. Saswata Hier-Majumder for his continuous support and guidance during this research. I would also like to thank the other members of my committee: Prof. Wenlu Zhu and Prof. Sarah Penniston-Dorland, as well as Prof. Laurent Montési, for their insightful comments and assistance. Special thanks are also given to the graduate students in the geodynamics group: Jodi Gaeman, Tyler Drombosky, Kevin Miller, Minjin Baek, and Stephanie Johnston, who all have assisted me multiple times during my graduate research. Finally, I would like to thank my friends and family who have supported me throughout my education. I would especially like recognize Justin DeSha-Overcash, whose friendship has been invaluable.

# Table of Contents

<b>1</b>	<b>Introduction</b>	<b>1</b>
1.1	Melting in the Earth's interior . . . . .	3
1.2	Microstructure in partially molten rocks . . . . .	6
1.3	Effective physical properties of partially molten rocks . . . . .	8
1.4	Building the model . . . . .	10
<b>2</b>	<b>Methods</b>	<b>13</b>
2.1	Governing equations . . . . .	15
2.1.1	Steady-state grain shape . . . . .	16
2.1.2	Packing arrangement . . . . .	20
2.1.3	Prescription of surface tension . . . . .	21
2.2	Solution techniques . . . . .	22
2.2.1	Expansion in spherical harmonics . . . . .	23
2.2.2	Numerical integration . . . . .	24
2.3	Microstructural and mechanical properties . . . . .	26
2.3.1	Quantitative parameters describing the melt geometry . . . . .	26
2.3.2	Calculation of seismic velocities . . . . .	30
2.4	Error analysis and data modeling . . . . .	32
2.4.1	Power spectrum . . . . .	32
2.4.2	Error in grain volume and surface area measurement . . . . .	33
2.4.3	Goodness of fit measurement . . . . .	34
<b>3</b>	<b>Results</b>	<b>35</b>
3.1	Solutions for grain shape and melt geometry . . . . .	36
3.2	Melt fraction and contiguity in the unit cell . . . . .	39
3.3	Comparison with previous studies . . . . .	44
<b>4</b>	<b>Discussion</b>	<b>47</b>
4.1	Comparison with experimental data . . . . .	48
4.2	Seismic properties . . . . .	50
4.3	Implications for ULVZ . . . . .	53

<b>5 Conclusion</b>	<b>55</b>
<b>A Analytical solution for the flow field</b>	<b>57</b>
<b>B Prescription of contact faces</b>	<b>63</b>
<b>C Data table</b>	<b>66</b>

# List of Tables

2.1	Comparison of standard integrals between exact solutions, trapezoidal integral, and spline integral. . . . .	26
3.1	Parameters for fit to the contiguity ( $\psi$ ) as a function of melt fraction ( $\phi$ ). The fit is given by $\psi = p_1\phi^5 + p_2\phi^4 + p_3\phi^3 + p_4\phi^2 + p_5\phi + p_6$ . The entries in the second and third row indicate the error bounds to the parameters within 95% confidence bound. For the fit the value of the sum of squared errors and $R^2$ are $1.67 \times 10^{-4}$ and 0.9995, respectively. . . . .	44
C.1	Contiguity and melt fraction measurements . . . . .	67

# List of Figures

1.1	Cartoon depicting areas of melt within Earth's interior. The brown region corresponds to the lithosphere, the red region depicts the asthenosphere, the orange area gives the lower mantle, and the yellow region gives the core. Partial melting occurs at the Lithosphere-Asthenosphere boundary ( <i>Rychert et al.</i> , 2007), at the midmantle transition zone in a Low Velocity Layer ( <i>Courtier and Revenaugh</i> , 2007), and at ULVZ atop the CMB ( <i>Hier-Majumder</i> , 2008). . . . .	4
1.2	Flow chart depicting aspects of previous models as well as this model. . . . .	11
2.1	Packing arrangement of the grains. (a) An individual grain, with the areas of contact with other grains in dark color. The central grain in red is contiguous to 12 other grains, (b) six along the $\theta = \pi/2$ plane (shown in red), (c) three above at $\theta = \sin^{-1}(\sqrt{1/3})$ (shown in blue), and three below at an angle of $\theta = \pi - \sin^{-1}(\sqrt{1/3})$ (shown in green). . . . .	21
2.2	A schematic diagram of the colatitude $\theta$ and azimuthal angle $\phi$ defined with respect to Cartesian coordinates. . . . .	22
2.3	Map of the varying surface tension prescribed across the grain. The horizontal axis represents the colatitude $\theta$ and the vertical axis represents the azimuthal angle $\phi$ . The surface tension is prescribed with double step functions given by equation (2.20) and the value of surface tension at the white regions is equal $\gamma'_{gg}$ and black regions equal $\gamma'_{gm}$ . The grain-grain contacts are prescribed following the symmetry of a rhombic dodecahedron. The shapes of the grain-grain contacts are used to mimic the shape of rhombi on the surface of a rhombic dodecahedron. The value of $\theta'$ gives the center of contact patches above the equatorial plane, where $\sin\theta' = \sqrt{(1/3)}$ . . . . .	23



2.4	A schematic diagram depicting the unit cell in face-centered-cubic packing. Two sets of axes are marked in the diagram. The set $x, y, z$ refers to the local Cartesian reference frame whose $x - y$ plane is parallel to one of the stacking planes. The lattice parameters $a, b$ , and $c$ of the unit FCC cell are also marked in the plot. Indices on the grain center (in no particular order) depict the arrangement used in the code. . . . .	27
2.5	Packing arrangement of the grains in an FCC unit cell. Each color represents a different packing plane. Blue arrows indicate the unit cell vectors along the cube edges, while the green arrow is the normal to the planes. . . . .	28
2.6	A cross-section in the $x - y$ plane, displaying the relationship between the radius of the contact face and the decrease in distance between grain centers due to flattening. By measuring $\theta^*$ the value of $\delta$ and $w$ are found using equations (2.29) and (2.30), respectively. . . . .	29
3.1	Shape of a single grain, calculated from equation (2.19), and colored by the value of $f$ . A positive $f$ value, yellow and white, perturb the initial sphere by pushing out while a negative $f$ value, red and black, deform the sphere by pushing in and flattening the grain surface. The color scale is the same as given in Figure 3.2. Contacts with melt pockets, tubules, and junctions are marked on the grain. . . . .	37
3.2	Surface map of (a) the prescribed surface tension, and (b) perturbed shape of the grain. The two surface maps are related by equations (2.19) and (2.25). Higher values of surface tension correspond to negative values of $f$ , and perturb the initial sphere by flattening the grain surface, while a lower values of surface tension correspond to positive values of $f$ and deform the sphere by pushing out the grain surface, see Figure 3.1. . . . .	38
3.3	Melt tubules and pockets surrounding an individual grain for four different melt fractions. Red coloring represents grain-melt contact and green represents grain-grain contact. The melt volume fractions for the given configurations are (a) $\phi = 0.06$ , (b) $\phi = 0.11$ , (c) $\phi = 0.14$ , (d) $\phi = 0.22$ . . . . .	38
3.4	Melt tubule and three grains for four different melt fractions. From this view, the cross section of a melt tubule leading into a melt pocket is visualized. The color scale represents the value of $f$ , the perturbation in shape function. As the melt volume fraction increases, the channel grows larger, and the area of grain-grain contact decreases. The melt fractions for the given configurations are $\phi = 0.06$ , (b) $\phi = 0.11$ , (c) $\phi = 0.14$ , (d) $\phi = 0.22$ . . . . .	40

3.5	Melt tubule and three grains for four different melt fractions. From this view, the side of a melt tubule leading into a melt pocket is visualized. The color scale represents the value of $f$ , the perturbation in shape function. As the melt volume fraction increases, the tubule grows from a small tubule into a large pocket of melt. The melt fractions for the given configurations are $\phi = 0.06$ , (b) $\phi = 0.11$ , (c) $\phi = 0.14$ , (d) $\phi = 0.22$ . . . . .	41
3.6	Power spectrum of the norm squared of $\gamma_{l,m}$ . . . . .	41
3.7	A calculated multiparticle unit cell with an FCC geometry. The dimension of each unit cell parameters $a$ , $b$ , and $c$ are equal to 2.61, approximately 8% shorter than an FCC packed with solid spheres, for which, $a = b = c = 2.82$ . The volume of the unit cell is 17.72, while the volume of each grain is 4.19, leading to a melt volume fraction of 0.05. (a) The FCC unit cell with blue arrows indicating the edges of the cubic unit cell. The green arrow points in the direction of the normal to each close packed plane. (b) A view of the unit cell along the close packed planes.	43
3.8	Plots showing the effect $\epsilon$ has on (a) melt volume fraction and (b) contiguity. Increasing $\epsilon$ results in greater grain-grain contact area and a denser packing arrangement. Notice how the relationship between $\epsilon$ and melt volume fraction is nearly linear, while the relationship between $\epsilon$ and contiguity is nonlinear. . . . .	43
3.9	Comparison between contiguity from this work and the results of <i>von Bargen and Waff</i> (1986). The lines marked vBW86 and WHMfit corresponds to the model of <i>von Bargen and Waff</i> (1986) and the fit of our results, respectively. The results of <i>von Bargen and Waff</i> (1986) are limited to melt volume fractions below 0.05, but the fit is continued to higher melt fractions (dashed line). The red data points correspond to the results from this study. . . . .	45

4.1	Comparison between contiguity from this work, the results of <i>von Bargen and Waff</i> (1986), the experimental measurements of <i>Yoshino et al.</i> (2005), and the two dimensional model of <i>Hier-Majumder et al.</i> (2006). The results of <i>von Bargen and Waff</i> (1986) are limited to melt volume fractions below 0.05, but the fit is continued to higher melt fractions (dashed line). Extrapolation of the fit to our data is also plotted as a broken line. The circular data points and the triangular data points indicate measurements by <i>Yoshino et al.</i> (2005) of Olivine-MORB and KLB, respectively. The orange and blue curves represent the contiguity-melt fraction relationships determined by the study of <i>Hier-Majumder et al.</i> (2006) and <i>von Bargen and Waff</i> (1986), respectively. The red data points are results found in this study. The plot shows that two dimensional models, and experimental measurements dependent on two dimensional slices, result in higher values of contiguity than three dimensional models. . . . .	49
4.2	Plots of the changes in normalized shear and bulk modulus and the drop of seismic velocity of the partially molten rock as a function of melt volume fraction and contiguity. Plots (a) and (b) give the ratio between the effective bulk ( $K_{eff}$ ) and shear ( $N$ ) moduli and solid bulk ( $K$ ) and shear ( $\mu$ ) moduli in a partially molten aggregate as a function of melt volume fraction and contiguity, respectively. Plots (c) and (d) give the ratio of seismic velocities of a partially molten rock to the seismic velocities in the absence of melting as a function of melt volume and contiguity, respectively. The red and blue boxes in plot (c) give the range of observed velocity drops at the UltraLow Velocity Zone. . . . .	51
4.3	Ratio of seismic velocities of a partially molten rock to the seismic velocities in the absence of melting as a function of melt volume fraction. The seismic velocities from this study (solid lines) are compared to seismic velocities predicted by the two dimensional study of <i>Hier-Majumder et al.</i> (2006) (dotted lines). The horizontal red and blue boxes indicate the range of observed velocity drops at the Ultra-Low Velocity Zone. The vertical, shaded box is our predicted range of melt volume fraction, necessary to explain the observed seismic signature. . . . .	52
B.1	Parameters used to prescribe the size and shape of contact patches. . . . .	65

# Chapter 1

## Introduction

Partial melting of rocks influences their elastic properties and rheological behavior. As partial melting occurs, the melt pools along the grain edges, corners and boundaries. Along with the degree of melting, the geometry of this melt distribution, or melt microstructure, plays an important role in determining the effective physical properties of the rock (*Faul, 2001; Hier-Majumder, 2008; Hier-Majumder and Abbott, 2010; Hustoft and Kohlstedt, 2006; Scott and Kohlstedt, 2006; Takei, 1998, 2000, 2002; ten Grotenhuis et al., 2005; Yoshino et al., 2005*). As the volume fraction of melt in grain-edge tubules and pockets increases, the fractional area of intergranular contact, contiguity, decreases. Since the elastic strength of the load-bearing framework is controlled by contiguity, the effective bulk and shear moduli of partially molten rocks decrease with an increase in melt fraction. As the melt fraction reaches the threshold of disaggregation, intergranular contact is lost, and the effective shear modulus becomes zero (*Takei, 2002*). Thus, the velocity of shear waves is more sensitive to partial melting than that of  $P$  waves. In interpreting the melt volume fraction from observed differential reductions in seismic body wave velocities, a parameterization of contiguity-melt fraction relation is thus necessary.

The relation between contiguity and melt fraction has been studied in a number of theoretical and experimental studies. The seminal work of *von Bargen and Waff (1986)* explored the influence of melt fraction and dihedral angle on the three dimensional geometry of melt tubules and pockets for melt volume fractions up to 0.05. Experimental results, obtained from high resolution micrographs of polished sections of synthetic and natural rocks, investigate the relation between melt fraction and contiguity over a larger range of melt fraction and various dihedral angles (see *Yoshino et al. (2005)* for a compilation of data). Recently, X-ray microtomography has revealed direct visualization

of three dimensional melt distribution in a partially molten aggregates (*Zhu et al.*, 2011). Contiguity, however, is yet to be measured directly using this technique. Currently, the only measurement of contiguity at moderate to high melt fractions arise from two dimensional measurements or extrapolation of the three dimensional model of *von Bargar and Waff* (1986).

This work presents a new three dimensional dynamic model of melt microstructure that is able to predict contiguity for a given melt volume fraction. This study hypothesizes that the true behavior of the melt microstructure is best understood through a three dimensional study.

This chapter presents a brief background on the identified regions of melting in the Earth's interior, existing models of melt microstructure, the linkage between melt microstructure and effective physical properties, and an overview of the model used in this study.

## 1.1 Melting in the Earth's interior

The presence of partial melt in the Earth's deep interior is observed in a number of melt-rich zones and regions of melt extraction. For example, a patchwork of dense, melt-rich UltraLow Velocity Zones (ULVZ) have been detected above the Core-Mantle Boundary (CMB) (*Hutko et al.*, 2009; *Rost et al.*, 2005; *Wen and Helmberger*, 1998; *Williams and Garnero*, 1996). Seismic studies also suggests a modest amount of partial melt occurring atop the mantle transition zone in a Low Velocity Layer (LVL) (*Courtier and Revenaugh*, 2007; *Revenaugh and Sipkin*, 1994; *Tauzin et al.*, 2010; *Vinnik and Farra*, 2007) and possibly in a Low Velocity Zone (LVZ) at the Lithosphere-Asthenosphere Boundary (LAB) (*Fischer et al.*, 2010; *Kawakatsu et al.*, 2009; *Rychert et al.*, 2007). In dynamic regions of melting and melt migration, such

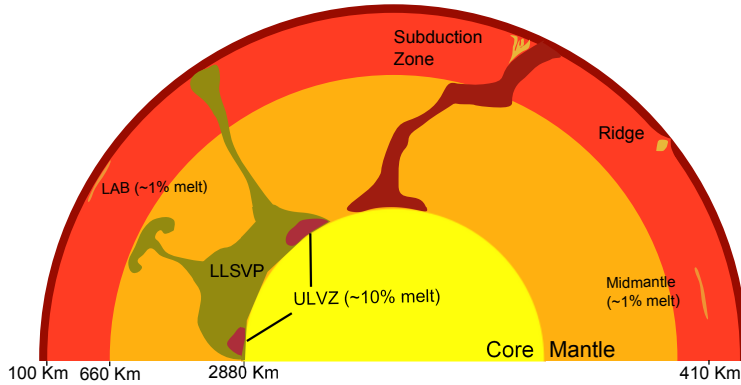


Figure 1.1: Cartoon depicting areas of melt within Earth’s interior. The brown region corresponds to the lithosphere, the red region depicts the asthenosphere, the orange area gives the lower mantle, and the yellow region gives the core. Partial melting occurs at the Lithosphere-Asthenosphere boundary (Rychert *et al.*, 2007), at the midmantle transition zone in a Low Velocity Layer (Courtier and Revenaugh, 2007), and at ULVZ atop the CMB (Hier-Majumder, 2008).

as subduction zones, midoceanic ridges, and plumes, the trajectory of melt is transient and spatially variable.

The schematic diagram in Figure 1.1 summarizes some of these regions of partial melting in the Earth’s interior. In the cartoon, the brown regions correspond to the lithosphere and a subducting slab, and red corresponds to the asthenosphere. Regions of partial melting in these areas are given by orange patches. The green region corresponds to a Large Low-Shear-Velocity Province (LLSVP). Two of these broad regions with lowered shear wave velocities and increased density have been detected by seismic studies, and together cover nearly half of the CMB (Garnero and McNamara, 2008). Along the edge of the LLSVP, thin patches of ULVZs have been detected. In the cartoon, the sizes of these structures are not to scale.

A number of studies identify regions with sharp drops of shear wave velocity at the LAB (Kawakatsu *et al.*, 2009; Rychert *et al.*, 2007). The LVZ can be explained by the presence of a modest amount of melt (Kawakatsu *et al.*, 2009)

which is dynamically stable at the LAB (*Hirschmann, 2010*). The presence of melting not only affects the seismic velocities of the region, but also the viscous coupling between the lithosphere and asthenosphere, which is essential for plate tectonics (*Fischer et al., 2010*).

Drop in shear wave velocity and impedance indicates the likely presence of a partially molten layer, varying in thickness between 30-90 km atop the 410 km discontinuity (*Courtier and Revenaugh, 2007; Revenaugh and Sipkin, 1994; Vinnik and Farra, 2007*), which may be global (*Tauzin et al., 2010*). The nature of melting in this zone is still unclear, although it is suggested that the seismic signature can be explained by carbonate melting (*Dasgupta and Hirschmann, 2006, 2010*). This layer has important consequences for the storage of radiogenic elements and can hold distinct geochemical reservoirs, which has implications to planetary evolution (*Bercovici and Karato, 2003*).

Sharp reductions of 10% and 30% in  $P$  and shear wave velocities, respectively, mark the presence of the ULVZ at the CMB (*Hutko et al., 2009; Rost and Revenaugh, 2003; Rost et al., 2005; Wen and Helmberger, 1998; Williams and Garnero, 1996*). This region is also 10% denser and likely two orders of magnitude weaker than the surrounding mantle (*Hier-Majumder and Revenaugh, 2009; Rost and Revenaugh, 2003*). The large drop in shear wave velocity in this region implies a much larger melt volume fraction than at the two shallower LVZ described above. Results from laboratory experiments indicate that iron-rich high pressure phases can explain some of the observed velocity reductions (*Mao et al., 2006; Wicks et al., 2010*). Explaining the seismic signature of the ULVZ by only iron-rich solids, however, is difficult to reconcile with a few other seismic and experimental observations. Occurrence of ULVZ beyond the stability field of iron-rich postperovskite (*Garnero and McNamara, 2008*), strong



iron depletion in magnesiowüstite in contact with outer core liquid (*Ozawa et al.*, 2008, 2009), and iron enrichment in silicate melt under conditions similar to the ULVZ (*Nomura et al.*, 2011), indicate that some extent of melting is likely to occur in the ULVZ.

A relatively large volume fraction of dense melt, however, is difficult to retain uniformly distributed within the ULVZ (*Hernlund and Tackley*, 2007), as the high density melt will tend to pool near the bottom of the ULVZ. *Hernlund and Jellinek* (2010) suggested stirring of the mushy ULVZ can prevent such a gravitational drainage. *Hier-Majumder et al.* (2006) suggest that capillary tension at grain-grain contact can reduce the drainage efficiency of the melt. Inferring the extent of melting from the seismic signature of the ULVZ, is thus crucial in understanding the internal dynamics of these structure, as well as the long term stability of mantle plumes (*Jellinek and Manga*, 2004) and the dynamics of the two LLSVPs in the base of the mantle (*McNamara et al.*, 2010).

## 1.2 Microstructure in partially molten rocks

In equilibrated, partially molten materials, a combination of processes, collectively termed ‘liquid phase sintering’, leads to the steady-state microstructure (*German*, 1985; *Kang*, 2005; *Kingery*, 1959). The process of liquid phase sintering consists of three main steps. First, grains are rearranged giving a denser packing arrangement. Next, flattening occurs at contact points between grains, which resulting in further densification. Finally, neighboring grains weld at contact points and a solid skeletal framework is formed (*Jurewicz and Watson*, 1985).

A number of theoretical models have investigated the microstructure in

partially molten rocks and liquid phase sintered ceramic materials. These models can be broadly classified into two groups. The first group focuses on a robust description of the melt geometry, neglecting the dynamic balance between surface tension, pressure, and viscous flow during liquid phase sintering (*German, 1985; Kang, 2005; Kingery, 1959; von Bargaen and Waff, 1986; Wray, 1976*). The second class of models incorporates the dynamics but has a poor geometric resolution (*Hopper, 1990, 1993a,b; Kuiken, 1993*).

Geometric models assume that melt resides along either grain edge tubules, grain corner pockets, or along grain boundaries (*Wray, 1976*). One of the most comprehensive models by *von Bargaen and Waff (1986)* assumes that the steady-state shape of the melt is determined by minimization of a scalar chemical potential, leading to a constant mean curvature. The dihedral angle,  $\theta$ , related to the grain-grain ( $\gamma_{gg}$ ) and grain-melt ( $\gamma_{gm}$ ) surface tensions via Young-Dupré relation

$$\cos \frac{\theta}{2} = \frac{\gamma_{gg}}{2\gamma_{gm}}, \quad (1.1)$$

is prescribed as a boundary condition in their model. As a result, the model can be perfectly matched at the boundary with the experimentally observed dihedral angles. However, the lack of stress, pressure, and variable curvature in such formulations prevent these models to be applicable for regions undergoing deformation, where microstructure is dynamic and the Young Dupré relation doesn't hold (*Hier-Majumder et al., 2004; Jansons, 1984*). A number of experimental and theoretical studies demonstrate that the microstructure of melt can be altered by the application of stress (*Daines and Kohlstedt, 1997; Holtzman et al., 2003; Katz et al., 2006; Zimmerman et al., 1999*) and the seismic properties can be altered by the reorientation of melt by deformation (*Takei, 2005*). In the lower mantle, ULVZ may experience stresses from an

upwelling flow in the surrounding mantle (*Rost et al.*, 2005).

In contrast, dynamic models involve one or two coalescing cylinders which deform under the influence of surface tension (*Hopper*, 1990, 1993a,b; *Kuiken*, 1993). The surface tension along the grain-melt interface excites a viscous flow within the grain, as well as within melt pockets, until a steady-state shape is reached. While the surface tension across the grain may be used to mimic surrounding grains, there is no imposed structure. In models which include more than one grain, the area of intergranular contact, contiguity, is not tracked because these models assume that all of the grains coalesce into one large grain. Consequently, contiguity and dihedral angle cannot be calculated from the steady-state grain-melt geometry. The inability to calculate these variables restricts the usefulness of these models in calculating effective physical properties of the partially molten rock and the results are not testable against laboratory measurements.

Unlike these previous models, this model describes the three dimensional, steady-state microstructure by incorporating viscous flow to a realistic geometrical model of an aggregate. Previous models which have used this method (*Hier-Majumder*, 2008; *Hier-Majumder and Abbott*, 2010) have been restricted to two dimensions. This thesis extends the scope of these models by incorporating three dimensional geometry.

### **1.3 Effective physical properties of partially molten rocks**

Traditionally, to measure the influence of melt geometry on the effective elastic properties of partially molten rocks, melt inclusions were modeled

within a continuum solid phase. The inclusions used in these models range from simple spherical inclusions (*Berryman*, 1980a) to interconnected tubes (*Mavko*, 1980). While tube models may be able to approximately model the interconnected regions along grain boundaries where melt resides, the actual microstructure in partially molten rocks is much more complex.

The inclusion models solve for effective elastic moduli in various ways using different parameters. The formulation by *Berryman* (1980a,b), for calculating effective elastic moduli in an aggregate containing spherical and ellipsoidal inclusions, combines continuum mechanics of elastic media with principles of scattering theory. The results from *Berryman* (1980a,b) depend on the aspect ratio of the inclusions and melt volume fraction. This model was able to predict elastic moduli that fell within the theoretical Miller and Hashin-Shtrikman bounds, but is limited in terms of the inherent melt geometry.

Solving for the effective elastic moduli for a rock with a network of cracks, *O'Connell and Budiansky* (1974) use a self consistent energy approach. This approach evaluates the effective elastic moduli by estimating the isothermal potential energy for the uncracked rock, cracked body, and the potential energy change due to the inclusion of the cracks. Since the melt fraction is related to the size and number of cracks, the elastic moduli are only dependent on the crack density. The results of the crack model agree with that of the ellipsoidal inclusion model of *Berryman* (1980b) when the aspect ratio is small enough.

The actual microstructure in partially molten rocks, however, is much more complex than simple inclusions. This prevents accurate comparisons between these models and experimental results. The equilibrium geometry model of *Takei* (1998, 2002), treats the partially molten rock as a granular aggregate and describes the microstructure in terms of the contiguity of the rock. The

contiguity of a partially molten rock is influenced by the melt volume fraction, dihedral angle, and the state of deformation. Unlike the melt inclusion models, therefore, the equilibrium geometry model is able to incorporate much more information to calculate the effective elastic moduli.

The model in this study predicts the contiguity of a partially molten rock in three dimensions as a function of melt volume fraction. Once the contiguity is determined, the equilibrium geometry model of *Takei* (2002) is used to calculate elastic moduli and seismic velocities. The calculated seismic velocities are then compared with observations to consider the degree of melting in the ULVZ.

## 1.4 Building the model

This model incorporates aspects from the previous models discussed in Section 1.3. Figure 1.2 presents a flow chart describing the various aspects of the model. The first box on top left contains the preliminary information needed to construct the model. Preliminary information includes the symmetry of the unit cell representing the partially molten aggregate. Data from mineral physics on the physical properties of the solid and the melt are needed for inputs to the model. Once this information is available, we derive a set of coupled mass and momentum conservation equations to simulate the liquid phase sintering process, described earlier. Finally, these conservation equations are combined to yield a partial differential equation, linking the shape of a grain to the dynamic forces of liquid phase sintering.

The third box describes the most significant component of this model. In this stage, we solve the equation governing the shape of an individual grain. Next, we calculate the resulting melt volume fraction and contiguity within

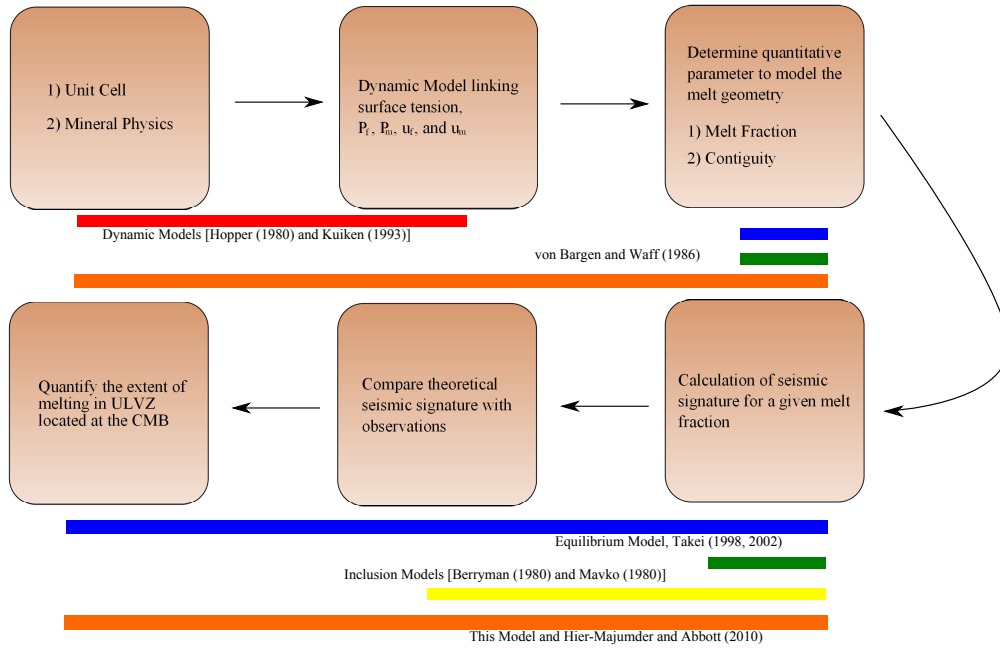


Figure 1.2: Flow chart depicting aspects of previous models as well as this model.

a unit cell consisting of grains of that shape. This stage is repeated multiple times with different control parameters to generate a data set consisting of a number of different melt volume fractions and the corresponding contiguities.

The fourth and fifth boxes illustrate the way the seismic signature of the rock is determined, and compares the results of the model with observation. We input the contiguity and melt fraction data generated in the previous step into the equilibrium geometry model to obtain a set of resultant effective elastic moduli and shear and  $P$  wave velocities. Comparing with the observed values, we can constrain the melt volume fraction in the ULVZ.

This model expands on the model of *Hier-Majumder* (2008) in which all of the six boxes in figure 1.2 were incorporated. The model of *Hier-Majumder* (2008), however, was restricted to two dimensions. In this study, a fully dy-

dynamic geometrical model is developed in three dimensions. Each grain is modeled using the rhombic dodecahedral symmetry. In this configuration, a grain is in contact with 12 other grains. From the steady-state grain shape, the microstructural parameters can be calculated. With these parameters the equilibrium geometry model of *Takei* (2002) is used to calculate seismic velocities which are used to quantify the extent of melting in the Earth's interior.

# Chapter 2

## Methods



The semianalytical technique in this thesis models the melt volume fraction, contiguity, and elastic properties averaged over a unit cell, consisting of 14 grains arranged in a face-centered-cubic (FCC) symmetry. Each grain in the unit cell is contiguous to 12 other grains, while the interstitial volume is saturated with melt. The surface tension on each grain varies spatially between grain-grain and grain-melt contacts. The spatial gradient of surface tension excites a response flow within the grains and the interstitial melt. When the forces arising from pressure, surface tension, and viscous deformation balance each other, steady-state geometry is attained. Once the steady-state shape of each individual grain is derived from the governing equation, we populate the unit cell with identical grains to calculate the melt volume fraction and contiguity.

To systematically study the variation of contiguity with melt volume fraction, we consider a reference unit cell. In this reference unit cell, each grain, described by a unit sphere, makes only point contacts with its neighbors. In this configuration, contiguity is zero, and the volume fraction of the interstitial space is approximately 0.26, the porosity of FCC packed spheres. In partially molten rocks, this melt fraction, termed the ‘disaggregation melt fraction’, or the ‘rheologically critical melt fraction’, is marked by a sharp reduction in viscosity (*Scott and Kohlstedt, 2006*). Next, we consider the influence of neighboring grains on each grain, via surface tension, as a perturbation to this reference state. As the perturbation increases, the grains become more faceted, increasing the area of intergranular contact. Due to faceting, it is possible to pack the grains into a smaller unit cell, reducing the volume fraction of interstitial space. We carried out a series of numerical experiments with different extents of perturbation in each experiment. We then measured the

melt fraction and contiguity in each experiment. Finally, we fit the contiguity-melt fraction data to obtain a relation between contiguity and melt volume fraction. This work does not incorporate anisotropic grain boundary energy and the influence of varying dihedral angle on contiguity.

The methods underlying each of these aspects of the model are discussed in sections 2.1, 2.2, and 2.3. The method of analyzing errors in our model are discussed in section 2.4.

## 2.1 Governing equations

A set of processes, collectively termed ‘liquid phase sintering’, leads to the development of the steady-state microstructure in partially molten aggregates (*German, 1985; Kang, 2005*). Typically, two classes of models describe the processes involved during sintering. The first body of work models mass transfer by diffusion dominated processes (*German, 1985; Kang, 2005; Kingery, 1959*). The second suite of models treat the diffusive mass flux in an average sense, and treats the motion excited within the grains and the melt during sintering via a set of mass and momentum conservation equations (*Hopper, 1990, 1993a,b; Kuiken, 1993*). The steady-state shape of the grains is thus a balance between surface tension forces and the viscous forces within the grain. This work follows the second suite of models. Since this model incorporates stresses, it can be easily extended to model anisotropic microstructure developed in the presence of an applied stress (*Hier-Majumder, 2011*), as expected in the dynamic interior of the Earth.

### 2.1.1 Steady-state grain shape

Consider a collection of grains in a partially molten unit cell. We express the steady-state shape of a grain as a small perturbation from a sphere. The shape function  $F_k$  describing the  $k^{th}$  particle is given by,

$$F_k = r - a(1 + \epsilon f_k) = 0, \quad (2.1)$$

where  $f_k$  is an unknown function arising from surface tension,  $a$  is the grain size, and the coefficient of deformation,  $\epsilon$ , is a constant. The variable  $r$  is the radial distance from the center of the grain. We notice that the unit normal to the grain  $\hat{\mathbf{n}}_k$  is given by (*Leal, 1992*),

$$\hat{\mathbf{n}}_k = \frac{\nabla F_k}{|\nabla F_k|} = \hat{\mathbf{r}} - \epsilon \nabla f_k. \quad (2.2)$$

where  $\hat{\mathbf{r}}$  is the unit radial vector.

In the reference state or zeroth order, velocities within each grain and the melt phase are considered zero. The pressure within each phase has a nonzero zeroth order component. Within the  $k^{th}$  grain ( $i = k$ ) or melt ( $i = m$ ), total dynamic pressure  $p_i^{total}$ , total velocity  $\mathbf{u}_i^{total}$ , and stress tensors  $\mathbf{T}_i^{total}$  are given by,

$$\mathbf{u}_i^{total} = \epsilon \mathbf{u}_i, \quad (2.3)$$

$$p_i^{total} = p_i^0 + \epsilon p_i, \quad (2.4)$$

$$\mathbf{T}_i^{total} = -p_i^{total} \mathbf{I} + \epsilon \mu_i (\nabla \mathbf{u}_i + \nabla \mathbf{u}_i^T), \quad (2.5)$$

where  $\mu_i$  is the viscosity and  $\mathbf{I}$  is the identity matrix.

In the perturbed state, the coupled flow within each grain and the melt

are governed by the conservation of mass and momentum within each particle and the melt. Each particle and the melt are treated as incompressible viscous fluids, leading to the first order equations,

$$0 = \mu_i \nabla^2 \mathbf{u}_i - \nabla p_i, \quad (2.6)$$

and

$$0 = \nabla \cdot \mathbf{u}_i. \quad (2.7)$$

To solve for the unknown velocities, pressures, and shape functions, we need to impose two sets of boundary conditions. First, the velocity is assumed to be continuous at the interface of the  $k^{th}$  particle, implying no-slip at this interface,

$$\mathbf{u}_k|_{F_k=0} = \mathbf{u}_m|_{F_k=0}. \quad (2.8)$$

Next, the continuity of traction across the interface  $F_k = 0$  requires (*Leal*, 1992, Ch. 5),

$$\Delta \mathbf{T}^k \cdot \hat{\mathbf{n}}^k + \tilde{\nabla} \gamma - \gamma \hat{\mathbf{n}}^k (\nabla \cdot \hat{\mathbf{n}}^k) = 0, \quad (2.9)$$

where  $\Delta \mathbf{T}^k$  is the stress drop on the surface of the  $k$ -th grain and  $\gamma$  is the interfacial tension. The surface gradient operator  $\tilde{\nabla}$  is defined as (*Manga and Stone*, 1995)

$$\tilde{\nabla} = [\mathbf{I} - \hat{\mathbf{n}}^k \hat{\mathbf{n}}^k] \cdot \nabla, \quad (2.10)$$

where  $\hat{\mathbf{n}}^k$  is the unit normal vector and  $\nabla$  is the gradient operator. The first term in the left hand side of the stress jump condition, equation (2.9), is the differential traction across the interface, the second term arises from the variation of interfacial tension on a grain, and the third term arises from curvature

driven surface tension force. The normal component of the stress jump condition is termed the Laplace condition while the tangential component is termed as Marangoni condition (*Hier-Majumder, 2008; Leal, 1992*). The total surface tension  $\gamma$  can also be expressed as a sum of the reference surface tension  $\gamma_0$  and a perturbation surface tension  $\gamma_1$ ,

$$\gamma = \gamma_0 + \epsilon\gamma_1. \quad (2.11)$$

The perturbation  $\gamma_1$  arises from the alteration of the surface properties due to contact with other grains. The nature of this function depends on the packing geometry of the grains and is discussed in section 2.1.3. Finally, the evolution of the shape of the  $k^{th}$  grain is governed by the kinematic relation (*Leal, 1992*),

$$\frac{\partial F_k}{\partial t} + \mathbf{u}_k \cdot \nabla F = 0. \quad (2.12)$$

Taken together, conservation equations (2.6) and (2.7), the no-slip boundary condition (2.8), normal component of the stress jump condition (2.9), and the kinematic condition (2.12) can be used to solve for the first order unknown velocity  $\mathbf{u}_i$ , pressure  $p_i$ , and shape perturbation of the  $k^{th}$  particle  $f_k$ . First, analytical solutions to the velocity and pressure fields are obtained using the technique of solid harmonics. Details of this technique is provided in Appendix A. Once the velocity and pressure fields are obtained, those solutions are substituted into the normal component of the stress jump condition 2.9 to obtain a second order partial differential equation in the unknown shape perturbation

$f_k$ . The above equations were nondimensionalized by using,

$$p_i = \frac{\mu_i u_0}{a} p'_i, \quad (2.13)$$

$$\mathbf{u}_i = u_0 \mathbf{u}'_i \quad (2.14)$$

$$\mathbf{r} = a \mathbf{r}' \quad (2.15)$$

$$\gamma = \gamma_0 \gamma', \quad (2.16)$$

where  $u_0$  is a reference velocity and  $\gamma_0$  is a reference value of grain-melt surface tension. The primes for the nondimensionalized parameters have been dropped for the following equations.

By analytically solving the above equations, explained in Appendix A, we obtain the evolution equation for the perturbed shape function  $f_k$ ,

$$\frac{\partial f_k}{\partial t} = \frac{2\gamma_0}{\mathcal{C}a(3+4\lambda)} \nabla^2 f_k - \frac{4\gamma_1}{\mathcal{C}a(3+4\lambda)}. \quad (2.17)$$

where  $\lambda$  represents the viscosity ratio between the grain and the melt,  $\mu_m/\mu_k$ , and  $\mathcal{C}a$  is the capillary number given by

$$\mathcal{C}a = \frac{\mu_k u_0}{\gamma_0} \quad (2.18)$$

which gives the relative magnitude of viscous and capillary forces at the interface. Once the steady-state is reached, the left hand side of equation (2.17) becomes zero, leading to the steady-state equation,

$$\nabla^2 f = \frac{2}{\gamma_0} \gamma_1, \quad (2.19)$$

where  $\gamma_0$  is constant. As evidenced by equation (2.19), in the steady-state,

only perturbation in the surface tension controls the perturbed grain shape. In the presence of an applied external stress, the grains and melt tubules deform continually, and equation (2.17) describes the shape evolution in a more appropriate manner. Notice, under such circumstances, the viscosity contrast between the grain and the melt and the capillary number influence the shape.

### 2.1.2 Packing arrangement

Two kinds of space-filling polyhedra are used to describe the grain shape in dense, multiparticle aggregates (*German, 1985; Lissant, 1966; Park and Yoon, 1985; von Bargaen and Waff, 1986*). While *von Bargaen and Waff (1986)* employed a truncated octahedral or tetrakaidecahedral geometry, *Park and Yoon (1985)* argued that a rhombic dodecahedron geometry is equally applicable for sintering models of multiphase materials. The work of *Lissant (1966)* argues that tetrakaidecahedral geometry is preferred for melt fractions below 0.06, and that the geometry of the rhombic dodecahedron is preferred for higher melt fractions. Later work of *Takei (1998)* also argues in favor of the rhombic dodecahedron geometry. This work explores the contiguity-melt fraction relation beyond the narrow range between 0 to 0.05 studied by *von Bargaen and Waff (1986)*. In addition, the equilibrium geometry model of *Takei (2002)* used to process the output of this model, is ideally suited for rhombic dodecahedral grains. Therefore, we selected rhombic dodecahedral symmetry to describe perturbed grains.

In the rhombic dodecahedron geometry, each grain has a coordination number of 12. The grain is surrounded by six other grains in its equatorial plane and three grains, offset from each other, each on the layer above and below

the equatorial layer, leading to an A-B-C packing arrangement. The diagram in Figure 2.1 outlines the coordination symmetry of a rhombic dodecahedral grain. This packing arrangement is used in the next section to prescribe the surface tension distribution of each grain.

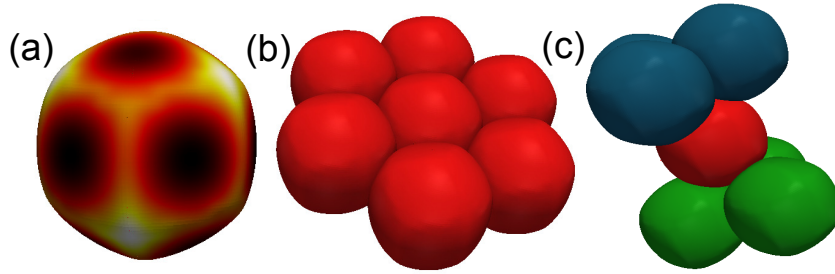


Figure 2.1: Packing arrangement of the grains. (a) An individual grain, with the areas of contact with other grains in dark color. The central grain in red is contiguous to 12 other grains, (b) six along the  $\theta = \pi/2$  plane (shown in red), (c) three above at  $\theta = \sin^{-1}(\sqrt{1/3})$  (shown in blue), and three below at an angle of  $\theta = \pi - \sin^{-1}(\sqrt{1/3})$  (shown in green).

### 2.1.3 Prescription of surface tension

Following *Takei* (1998), we identify 12 contact patches on each rhombic dodecahedral grain, where the perturbed surface tension is equal to  $\gamma'_{gg}$ , the grain-grain surface tension, and is equal to  $\gamma'_{gm}$  everywhere else:

$$\gamma_1(\theta, \phi) = (\gamma'_{gg} - \gamma'_{gm}) \sum_{i=1}^{12} h_i(\theta) g_i(\phi) \quad (2.20)$$

where  $h_i(\theta)$  and  $g_i(\phi)$  are combinations of step functions in  $\theta$  and  $\phi$ , the colatitude and the azimuthal angle, respectively. The schematic diagram in Figure 2.2 outlines the angles in the spherical coordinates. The difference in the two values of surface tension is used for the perturbation surface tension because  $\gamma_1$  is being added to the reference value of surface tension. The step



functions are used to model contact patches on the grain surface. This allows for equation (2.20) to be separated into its  $\theta$  and  $\phi$  components. Multiple step functions are used for each contact face to create the shape of a rhombus, see Figure 2.3 and Appendix B.

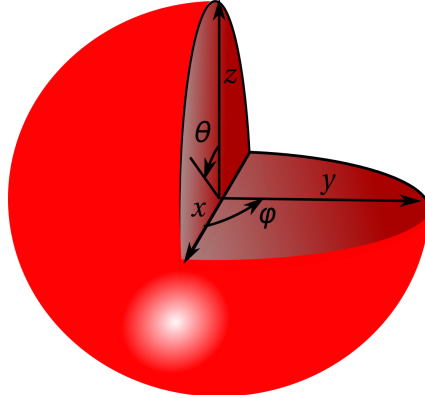


Figure 2.2: A schematic diagram of the colatitude  $\theta$  and azimuthal angle  $\phi$  defined with respect to Cartesian coordinates.

## 2.2 Solution techniques

This model provides solutions for perturbed pressure and velocity within each grain and the melt as well as the perturbed shape of the grains. Solution to the velocity and pressure fields were obtained analytically using the method of solid harmonics. Analytical solution building technique for these fields are described in Appendix A. Due to the nature of the perturbed surface tension,  $\gamma_1$  described in equation (2.20), equation (2.19) was solved numerically by using a spherical harmonic transform. The following subsections derive the solution building method for the perturbed shape function  $f_k$  of the  $k^{th}$  particle, outlines the numerical methods, and discusses the errors associated.

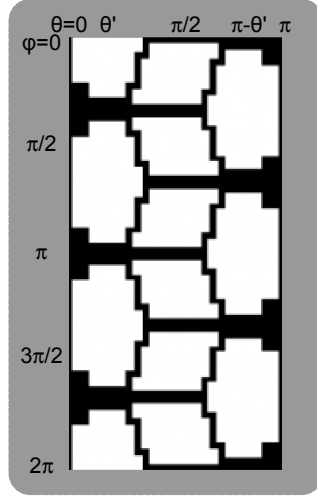


Figure 2.3: Map of the varying surface tension prescribed across the grain. The horizontal axis represents the colatitude  $\theta$  and the vertical axis represents the azimuthal angle  $\phi$ . The surface tension is prescribed with double step functions given by equation (2.20) and the value of surface tension at the white regions is equal  $\gamma'_{gg}$  and black regions equal  $\gamma'_{gm}$ . The grain-grain contacts are prescribed following the symmetry of a rhombic dodecahedron. The shapes of the grain-grain contacts are used to mimic the shape of rhombi on the surface of a rhombic dodecahedron. The value of  $\theta'$  gives the center of contact patches above the equatorial plane, where  $\sin\theta' = \sqrt{1/3}$ .

### 2.2.1 Expansion in spherical harmonics

The perturbed shape of the  $k^{th}$  particle  $f_k$  is forced by the perturbed surface tension  $\gamma_1$  in the governing equation (2.19). We can express the unknown function  $f_k$  and the known function  $\gamma_1$  as a sum of spherical harmonic functions, given by,

$$f_k = \sum_{m=0}^{\infty} \sum_{l=-m}^m f_{l,m} Y_l^m(\theta, \phi) \quad (2.21)$$

and

$$\gamma_1 = \sum_{m=0}^{\infty} \sum_{l=-m}^m \gamma_{l,m} Y_l^m(\theta, \phi) \quad (2.22)$$

where the spherical harmonic function  $Y_l^m$  is given by

$$Y_l^m(\theta, \phi) = (-1)^m \sqrt{\frac{2l+1}{2} \frac{(l-m)!}{(l+m)!}} P_l^m(\cos \theta) \exp(im\phi), \quad (2.23)$$

where  $P_l^m(\cos \theta)$  is the associated Legendre polynomial. To solve for the coefficient  $f_{l,m}$ , first we substitute the right hand sides of equations (2.21) and (2.22) into equation (2.19). The relationship,

$$r^2 \nabla^2 Y_l^m(\theta, \phi) = -l(l+1) Y_l^m(\theta, \phi) \quad (2.24)$$

is then used to relate the unknown coefficient  $f_{lm}$  to  $\gamma_{lm}$  by

$$f_{l,m} = -\frac{2}{\gamma_0 l(l+1)} \gamma_{l,m}. \quad (2.25)$$

By expanding the surface tension given by equation (2.20) into a spherical harmonic series (2.22), the steady-state shape function can be solved. As described in the following subsection, the coefficients in the expansion of surface tension  $\gamma_{l,m}$  are obtained numerically by taking the spherical harmonic transform of the expansion given in equation (2.22). From the dodecahedral symmetry of the contact function, the coefficients of the spherical harmonic expansion are non-zero only when  $l$  is even and  $m$  is a multiple of 3 (*Takei, 1998*). In the following subsection we discuss the numerical techniques used to evaluate these coefficients.

## 2.2.2 Numerical integration

Coefficients in the expansion of the prescribed surface tension,  $\gamma_1$  are obtained by taking the spherical harmonic transform of equation (2.22). First

we equate the right hand sides of equations (2.20) and (2.22) to get

$$\sum_{m=0}^{\infty} \sum_{l=-m}^m \gamma_{l,m} Y_l^m(\theta, \phi) = (\gamma'_{gg} - \gamma'_{gm}) \sum_{i=1}^{12} h_i(\theta) g_i(\phi). \quad (2.26)$$

To solve for the  $\gamma_{l,m}$  coefficients, the orthonormality condition of the spherical harmonic function is used,

$$\int_{\theta=0}^{2\pi} \int_{\phi=0}^{\pi} Y_{l_1}^{m_1}(\theta, \phi) Y_{l_2}^{m_2*}(\theta, \phi) \sin(\theta) d\theta d\phi = \delta_{l_1 l_2} \delta_{m_1 m_2}, \quad (2.27)$$

where  $Y_l^{m*}$  is the complex conjugate of the spherical harmonic function and  $\delta_{i,j}$  is the Kronecker delta function. Multiplying both sides of equation (2.26) by  $Y_l^{m*}(\theta, \phi)$ , integrating over the surface, and applying the orthonormality condition (2.27), we get the following equation for the coefficients in the spherical harmonic expansion of the perturbation in surface tension:

$$\gamma_{l,m} = (\gamma'_{gg} - \gamma'_{gm}) \sum_{i=1}^{12} \int_{\theta} \int_{\phi} h_i(\theta) g_i(\phi) Y_l^{m*}(\theta, \phi) \sin(\theta) d\theta d\phi. \quad (2.28)$$

Since the integrand in equation (2.28) is separable in  $\theta$  and  $\phi$ , the final integral can be evaluated as the product of two line integrals, one in  $\theta$  and one in  $\phi$ . Two separate numerical integration techniques, trapezoidal and spline integration, were used to evaluate the line integrals (*Press et al.*, 1992).

In the trapezoidal integration routine, the domain is divided in a number of equidistant elements. The resulting integral is then evaluated assuming a linear variation of the integrand within each element. In contrast, the spline integral, the domain was divided in a number of not necessarily equally spaced elements. Integration within each element was carried out using the Gaussian quadrature rule, distributed over 8 points. The value of the integrand, as well as the integration variable was interpolated to the quadrature points using a

Integral	Exact	Trapezoidal	Spline
$\int x^2 dx, x = 0, 2$	2.667	2.415	2.667
$\int x^3 dx, x = 0, 2$	4.000	3.644	4.000
$\int \exp^{(ix)} dx, x = 0, \pi$	$0.000 + 2.000 i$	$0.000 + 1.782i$	$0.000 + 2.001i$

Table 2.1: Comparison of standard integrals between exact solutions, trapezoidal integral, and spline integral.

second order spline interpolation. All numerical calculations were performed in double precision, using Intel FORTRAN 90 compilers in an SGI Altix 1300 cluster. Both integration routines were benchmarked for purely real as well as imaginary integrands. The results from some standard integrals are listed in table 2.1. We chose to employ the higher accuracy, spline integral routine to evaluate the integrations in  $\theta$  and  $\phi$ .

## 2.3 Microstructural and mechanical properties

### 2.3.1 Quantitative parameters describing the melt geometry

The melt volume fraction for the model was calculated from the geometry of the unit cell. As explained in section 2.1.2 each grain is surrounded by six grains in the equatorial plane ( $\theta = \pi/2$ ), three grains above the equatorial plane, and three grains below the equatorial plane. Each layer of grains above and below the equatorial plane is offset from each other, leading to a face

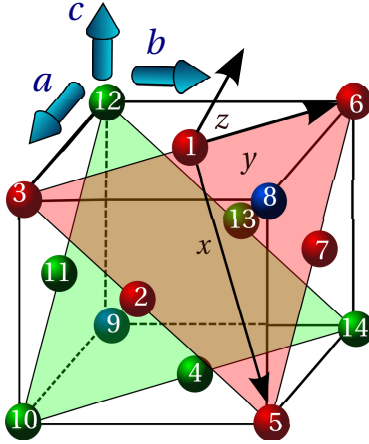


Figure 2.4: A schematic diagram depicting the unit cell in face-centered-cubic packing. Two sets of axes are marked in the diagram. The set  $x, y, z$  refers to the local Cartesian reference frame whose  $x - y$  plane is parallel to one of the stacking planes. The lattice parameters  $a, b$ , and  $c$  of the unit FCC cell are also marked in the plot. Indices on the grain center (in no particular order) depict the arrangement used in the code.

centered cubic (FCC) packing symmetry. The arrangement of the grains, including their indices (in no particular order), in an FCC lattice are depicted in Figures 2.4. The FCC packing arrangement is given in Figure 2.5 for full grains. If each grain was a perfect, unit sphere, similar to the unperturbed state, cell parameters  $a, b$ , and  $c$  of this unit cell would be equal to  $2\sqrt{2}$ . Assuming the empty space between the grains is saturated by melt, the melt volume fraction in this case would be 0.26.

We calculated the area of nearly circular grain-grain contact by measuring the radius of the contact. The radius,  $w$ , and the shortening  $\delta$ , displayed in Figure 2.6, vary linearly with the magnitude of the perturbation coefficient  $\epsilon$ ,

$$\delta = \epsilon \left( 1 - \cos \frac{\theta^*}{2} \right), \quad (2.29)$$

$$w = \epsilon \sin \frac{\theta^*}{2}, \quad (2.30)$$

where  $\theta^*$  is the angle subtended by an arc of contact in the cross section

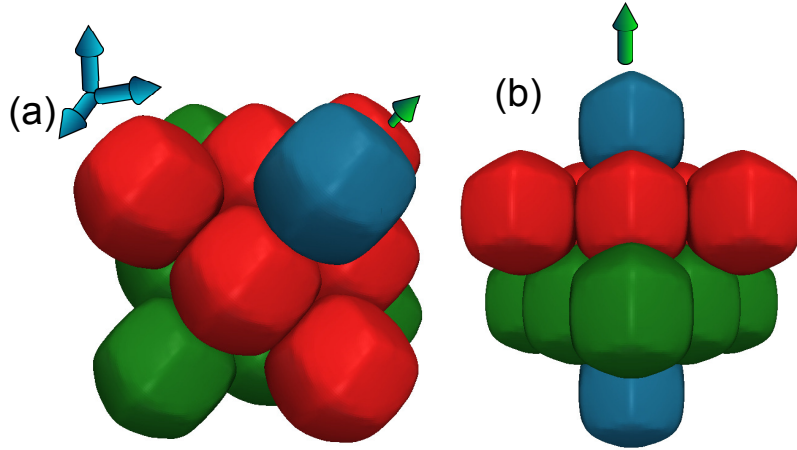


Figure 2.5: Packing arrangement of the grains in an FCC unit cell. Each color represents a different packing plane. Blue arrows indicate the unit cell vectors along the cube edges, while the green arrow is the normal to the planes.

displayed in Figure 2.6. In the absence of perturbation ( $\epsilon = 0$ ) both  $w$  and  $\delta$  are zero, rendering zero contiguity at the disaggregation melt fraction. From the numerical solution of varying  $f_k$  on the surface of the  $k^{th}$  particle, the boundary of this circle is marked by the contour of  $f_k = 0$ , the line of zero perturbation.

If the radius of the unperturbed sphere is shortened by an amount  $\delta$  at the center of a contact face, then the distance between the centers of two unit spheres is reduced to  $2(1 - \delta)$ . Knowing the location of the centers of the touching, flattened grains, we calculate the volume of the unit cell. Next, we calculate the volume of each grain numerically by using the software ParaView. The total volume of solids in each FCC unit cell is equal to 4 times the volume of one individual grain ( $8 \times \frac{1}{8}$  corner grains +  $6 \times \frac{1}{2}$  face centered grains = 4 grains). Thus, the melt fraction is calculated assuming the void within the unit cell is completely saturated by melt.

In successive numerical experiments, we varied the parameter  $\epsilon$  between 0.1 and 1. For each of the runs, we set the nondimensional surface tension

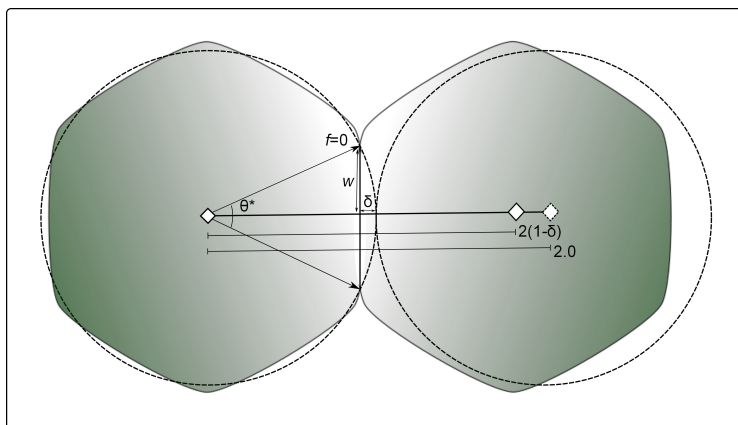


Figure 2.6: A cross-section in the  $x - y$  plane, displaying the relationship between the radius of the contact face and the decrease in distance between grain centers due to flattening. By measuring  $\theta^*$  the value of  $\delta$  and  $w$  are found using equations (2.29) and (2.30), respectively.

parameters,  $\gamma'_{gm} = 0.1$  and  $\gamma'_{gg} = 0.5$ . We carried out a total of 20 numerical experiments. In all simulations, the magnitude of the maximum perturbation to the shape, was always  $O(10^{-2})$ . These maximum values of perturbations were associated with flattened intergranular contacts and bulged melt-grain contacts. The small values of perturbation justify the underlying linear analysis, in which term  $O(\epsilon^2)$  or higher were neglected. The data on contiguity and melt fraction from these experiments were then fit with a polynomial function to obtain a melt fraction-contiguity relation between melt fractions of 0 and the disaggregation melt fraction.

Once the numerical solution for the perturbed shape functions are obtained, we calculated contiguity,  $\psi$ , of the faceted grain as the sum of area fraction of the 12 contact patches,

$$\psi = \frac{1}{4\pi} \sum_{i=1}^{12} A_i, \quad (2.31)$$

where  $A_i$  is the area of an individual patch.



### 2.3.2 Calculation of seismic velocities

Seismic signature and the effective bulk and shear moduli of a partially molten aggregate is controlled by the contiguity,  $\psi$ , and melt volume fraction  $\phi$ . Velocity of seismic waves traveling through the aggregate is controlled by the effective elastic moduli, as well as the liquid volume fraction,  $\phi$ . In this study, the equilibrium geometry model, proposed by *Takei* (2002) is used to calculate the effective elastic moduli and seismic velocities of a partially molten rock. The ratio between the shear and  $P$  wave velocities through the partially molten aggregate,  $V_s$  and  $V_P$ , to the velocities in the solid  $V_{S0}$  and  $V_{P0}$  are given by,

$$\frac{V_S}{V_{S0}} = \sqrt{\frac{(N/\mu)}{(\bar{\rho}/\rho)}}, \quad (2.32)$$

and

$$\frac{V_P}{V_{P0}} = \sqrt{\frac{K_{eff}/K + 4\beta/3(N/\mu)}{(1 + 4\beta/3)(\bar{\rho}/\rho)}}, \quad (2.33)$$

where  $K, \mu$  and  $\rho$  are the bulk modulus, shear modulus, and density of the solid, and  $\beta = \mu/K$ . The quantity  $\bar{\rho}$  and  $K_{eff}$  is the volume averaged density and effective bulk modulus of the grain-melt aggregate, and  $N$  is the shear modulus of the intergranular skeletal framework. The skeletal framework represents the solid framework with vacuum pores. To evaluate the effective elastic moduli at core-mantle boundary conditions, the bulk modulus, shear modulus, and density of the solids were obtained from the Preliminary Reference Earth Model (PREM). We also assumed that the density of the melt is equal to that of the solid under this condition (*Mosenfelder et al.*, 2007; *Stixrude and Karki*, 2005).

The presence of melt affects  $V_P$  and  $V_S$  differently. This results in changes of

$V_P/V_S$  ratio for seismic signals passing through a system containing melt. If the elasticity of the solid phase are known,  $V_S$  can be determined by melt volume fraction  $\phi$  and contiguity  $\psi$ . To determine  $V_P$ , however, the compressibility of the liquid phase must be taken into account (*Takei, 2000*). The  $V_P/V_S$  is given by combining (2.32) and (2.33)

$$\frac{V_S/V_{S0}}{V_P/V_{P0}} = \frac{\sqrt{N/\mu}\sqrt{(1+4\beta/3)}}{\sqrt{K_{eff}/K + 4\beta/3(N/\mu)}} \quad (2.34)$$

The elastic moduli can be expressed in terms of melt volume fraction  $\phi$  and contiguity  $\psi$  as

$$N = \mu(1-\phi)g(\psi) \quad (2.35)$$

$$K_{eff} = K \left[ (1-\phi)h(\psi) + \frac{(1-(1-\phi)h(\psi))^2}{(1-\phi)(1-h(\psi)) + \phi K/K_m} \right], \quad (2.36)$$

where  $K_m$  is the bulk modulus of the melt, which gives the compressibility of the melt needed to calculate  $V_P$ . The functions  $g(\psi)$  and  $h(\psi)$  are given by,

$$g(\psi) = 1 - (1-\psi)^n, \quad (2.37)$$

$$h(\psi) = 1 - (1-\psi)^m, \quad (2.38)$$

where  $n$  and  $m$  are also dependent on contiguity  $\psi$  (*Takei, 2002, Appendix A*). It can be seen that in a system with zero melt,  $\phi = 0$ , and complete contact between grains,  $\psi = 1$ , the shear and bulk moduli of the aggregate become the same as the moduli of the solid phase.

Finally, the bulk modulus of the melt under the core-mantle boundary

condition were evaluated using a linear equation of state,

$$K_m = K_m^0 + K'P, \quad (2.39)$$

where values of the bulk modulus at the surface,  $K_m^0 = 114.8$  GPa, and the pressure derivative  $K' = 2.9$  (GPa/GPa) were obtained for HPP melt data reported by *Mosenfelder et al.* (2007). Using a pressure of 136 GPa, the liquid bulk modulus of 509.2 GPa was obtained for the core-mantle boundary. Since the solid values are estimated from the PREM model, all calculated seismic anomalies are in reference to the PREM model.

## 2.4 Error analysis and data modeling

In this section, we discuss various sources of error and the analysis of these errors. Three major sources of error exist in the current analysis. First, the infinite series expansion in spherical harmonics is truncated to a finite number of terms, leading to some error in the approximated function. Second, in the numerical code, total volume and surface area of each grain is considered equal to that of a unit sphere, also leading to some error in the measurements. Finally, the data set of melt volume fraction and contiguity was fit to a polynomial function. The goodness of fit and associated errors need to be considered.

### 2.4.1 Power spectrum

A power spectrum is constructed for the coefficients in the spherical harmonic expansion of the surface tension. Theoretically, this expansion is done on an infinite series. Truncation to finite terms introduces errors in the approximation made by the spherical harmonic expansion. We controlled the

magnitude of this error by calculating the power spectrum of the expansion. The power spectrum is created by taking the sum of the squares of the coefficients for each degree  $l$ :

$$S_{ff}(l) = \sum_{m=-l}^l \gamma_{lm}^2. \quad (2.40)$$

Since high orders of  $l$  are used to investigate small-scale structures, it is expected that  $S_{ff}(l)$  will decrease as  $l$  is increased. To save computational time, we can use the power spectrum to find a value for  $l$  at which we can truncate the infinite series used in the spherical harmonic transform. We choose to truncate the series when  $S_{ff}$  falls below  $10^{-5}$ .

#### 2.4.2 Error in grain volume and surface area measurement

Calculating the contiguity and melt volume fraction of the aggregate, the surface area and volume of the grain are needed. In our calculations, it is assumed that the surface area and volume of the grain are the same as that of a unit sphere, an unperturbed grain. As the grains become closer, however, the surface of the grain flattens at grain-grain contacts and bulges out at grain-melt contacts. This changes the surface area and the volume of the grain. The software ParaView is used to numerically calculate the surface area and the volume. The errors in measuring grain volume and surface area are extrapolated to calculate our uncertainty in melt volume fraction and contiguity and are given in Appendix C.

### 2.4.3 Goodness of fit measurement

To fit our results to a curve of contiguity as a function of melt volume fraction, MATLABs curve fitting tool box is used. The toolbox supplies multiple formulas to be used to fit data and allows for the coefficients in the fit to be bounded. A 5<sup>th</sup> order polynomial of the form  $\psi = p_1\phi^5 + p_2\phi^4 + p_3\phi^3 + p_4\phi^2 + p_5\phi + p_6$  is chosen for our data set. The coefficient  $p_6$  is set to 1.0 so that when there is zero melt in the system, the contiguity of the grains is equal to one. On output of the fit, the toolbox also supplies goodness of fit measurements. This includes the 95% confidence bounds for each coefficient, the sum of squared errors ( $SSE$ ), and the values of  $R^2$ .  $SSE$  is given by:

$$SSE = \sum_{i=1}^n (y_i - f(x_i))^2, \quad (2.41)$$

where  $n$  is the number of measurements,  $y_i$  is  $i^{th}$  value of the measured contiguity,  $x_i$  is  $i^{th}$  value of measured melt fraction, and  $f(x_i)$  is the predicted value of  $y_i$ . To calculate the values of  $R^2$  for the fit, the total sum of squares ( $SST$ ) is needed:

$$SST = \sum_{i=1}^n (y_i - \bar{y}_i)^2, \quad (2.42)$$

where  $\bar{y}_i$  is the mean of the measured values of contiguity. The value of  $R^2$  is given by

$$R^2 = 1 - \frac{SSE}{SST}. \quad (2.43)$$

# Chapter 3

## Results

This section outlines the model results. First, the solution to the shape perturbation function under an applied surface tension is discussed. Next, the results for the melt volume fraction and contiguity in a unit cell are discussed. Finally, we compare the melt fraction-contiguity relation from our results with the results of three dimensional numerical simulation from *von Bargaen and Waff* (1986).

### 3.1 Solutions for grain shape and melt geometry

In the multiparticle aggregate, spatially varying surface tension leads to the flattening of the grain at intergranular contacts and bulging out at grain-melt contacts. The surface of a single grain, colored by the magnitude of the perturbed shape function  $\epsilon f$ , is visualized in Figure 3.1. Dark values indicate regions of flattening. Bright patches on the surface of each grain represent contact with three different kinds of melt units. Tubules are linear grain-melt contacts, located between two dark intergranular contacts. Pockets are situated between four contiguous dark intergranular contacts and at the intersection of four tubules. Finally, three tubules meet each other at junctions, which are situated at the intersection of three grain-grain contact patches. In this geometry, each grain has a total of 6 pockets, 8 junctions, and 24 tubules along the 24 edges of the rhombic dodecahedron.

Surface tension forces perturbation of the grain shape. The colormap in Figure 3.2 depicts the prescribed surface tension and the resulting perturbation of the reference shape in the  $\theta - \phi$  space. The accompanying colorbars indicate the magnitude of the perturbation to both the prescribed surface ten-

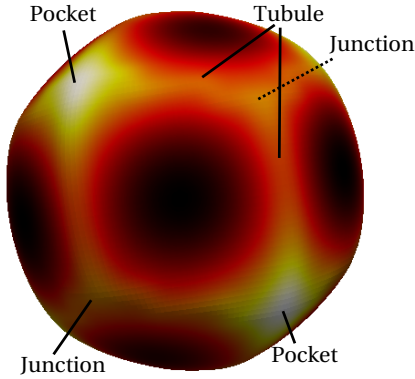


Figure 3.1: Shape of a single grain, calculated from equation (2.19), and colored by the value of  $f$ . A positive  $f$  value, yellow and white, perturb the initial sphere by pushing out while a negative  $f$  value, red and black, deform the sphere by pushing in and flattening the grain surface. The color scale is the same as given in Figure 3.2. Contacts with melt pockets, tubules, and junctions are marked on the grain.

sion and the shape. Since the prescribed surface tension assumes only two values, the color on Figure 3.2(a) is binary. As indicated by the surface plot in Figure 3.1, negative relief corresponds to regions of flattening. Tension on the intergranular contact flexes the grain surface inwards while slight bulges are produced at the grain-melt contact. It can also be seen from figures 3.1 and 3.2 that the contact patches given by the shape function  $f$  are more circular compared to the rhombus shaped patches of surface tension prescribed by equation (2.20). These contact patches are similar to the direct prescription of the patch geometry by *Takei* (1998).

Figure 3.3 shows melt tubules, junctions, and pockets that form around an individual grain for systems with different melt volume fractions. The melt volume fraction increases from Figure 3.3(a) to Figure 3.3(d) from 0.06 to 0.22. For clarity, two junctions and pockets are identified on Figure 3.3(a). The figures illustrate that as the melt volume fraction increases, the melt tubules and pockets grow larger, and the area of the circular grain-grain contacts decreases. The contiguity in the figures decrease from 0.38 in Figure 3.3(a) to



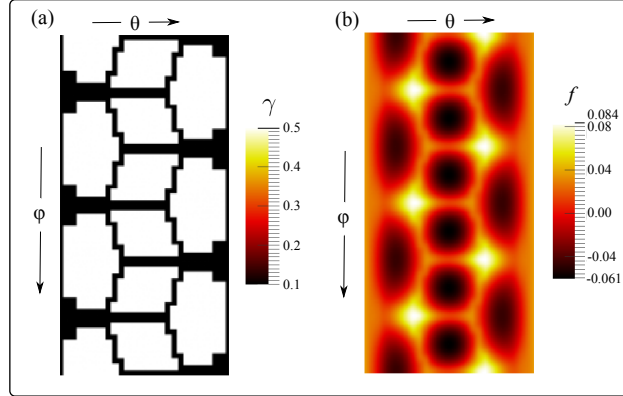


Figure 3.2: Surface map of (a) the prescribed surface tension, and (b) perturbed shape of the grain. The two surface maps are related by equations (2.19) and (2.25). Higher values of surface tension correspond to negative values of  $f$ , and perturb the initial sphere by flattening the grain surface, while a lower values of surface tension correspond to positive values of  $f$  and deform the sphere by pushing out the grain surface, see Figure 3.1.

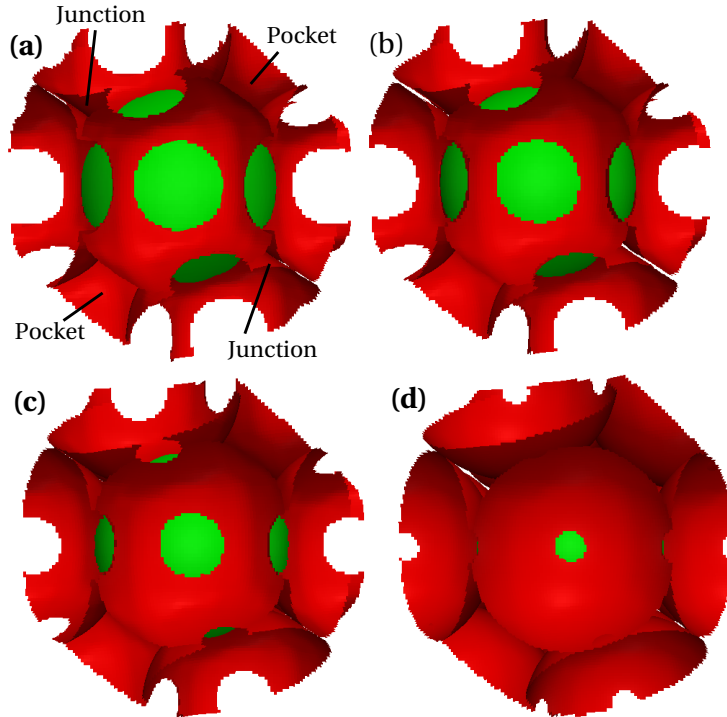


Figure 3.3: Melt tubules and pockets surrounding an individual grain for four different melt fractions. Red coloring represents grain-melt contact and green represents grain-grain contact. The melt volume fractions for the given configurations are (a)  $\phi = 0.06$ , (b)  $\phi = 0.11$ , (c)  $\phi = 0.14$ , (d)  $\phi = 0.22$ .

0.02 in Figure 3.3(d). The values of melt volume fractions and contiguity for all numerical experiments are described in the table in Appendix C.

We also compare the change in shapes of grains and tubules as the melt volume fraction increases, in Figures 3.4 and 3.5, depicting a melt tubule along with three grains from two different orientations. The melt volume fraction also increases from 0.06 to 0.22 in these figures. The colormap on the surface of the grains represent the magnitude of the perturbed shape function. Two features of the microstructure become clear as the melt volume fraction increases. First, the area of tubule cross-section increases with an increase in melt volume fraction. Second, the grains become less faceted and more round-shaped. The colormap on the grain surface, corresponding to the shape perturbation, becomes even as the melt fraction increases.

By numerically solving the coefficients in the spherical harmonic expansion of the surface tension,  $\gamma_{l,m}$  with equation (2.28), equation (2.25) may be solved. The infinite spherical harmonic series is truncated at  $l = 50$ . As the plot of power spectrum in Figure 3.6 suggests, contributions from higher order harmonics are negligible and increases the computational expense of the simulations.

## 3.2 Melt fraction and contiguity in the unit cell

In the perturbed state, the unit cell of the rhombic dodecahedron is substantially smaller when compared to a FCC packed unit cell of spheres. The surface plots in Figure 3.7 visualizes a unit cell from two different orientations. In Figure 3.7(a) blue arrows indicate the unit cell vectors in the FCC lattice. For a unit sphere, all three lattice parameters are equal to a uniform value of 2.82. In the perturbed state, the distance between the centers of the contigu-

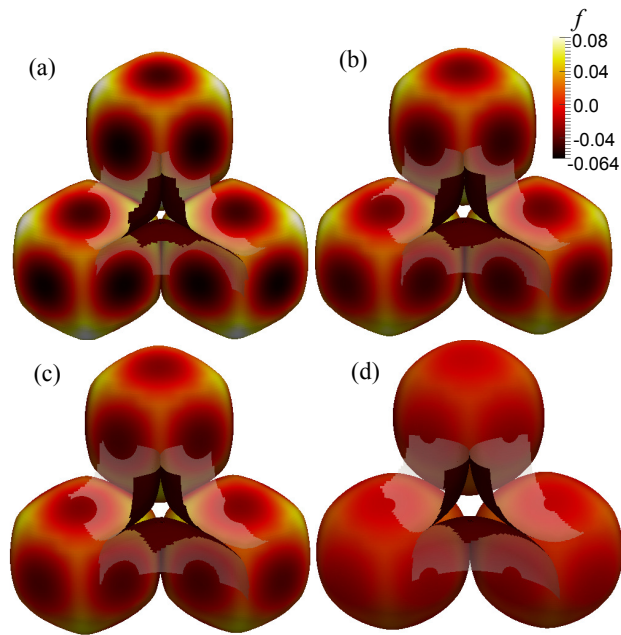


Figure 3.4: Melt tubule and three grains for four different melt fractions. From this view, the cross section of a melt tubule leading into a melt pocket is visualized. The color scale represents the value of  $f$ , the perturbation in shape function. As the melt volume fraction increases, the channel grows larger, and the area of grain-grain contact decreases. The melt fractions for the given configurations are  $\phi = 0.06$ , (b)  $\phi = 0.11$ , (c)  $\phi = 0.14$ , (d)  $\phi = 0.22$ .

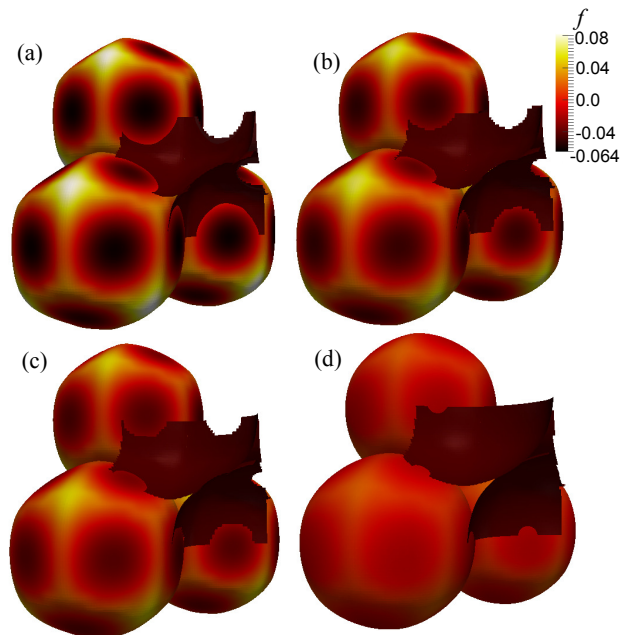


Figure 3.5: Melt tubule and three grains for four different melt fractions. From this view, the side of a melt tubule leading into a melt pocket is visualized. The color scale represents the value of  $f$ , the perturbation in shape function. As the melt volume fraction increases, the tubule grows from a small tubule into a large pocket of melt. The melt fractions for the given configurations are  $\phi = 0.06$ , (b)  $\phi = 0.11$ , (c)  $\phi = 0.14$ , (d)  $\phi = 0.22$ .

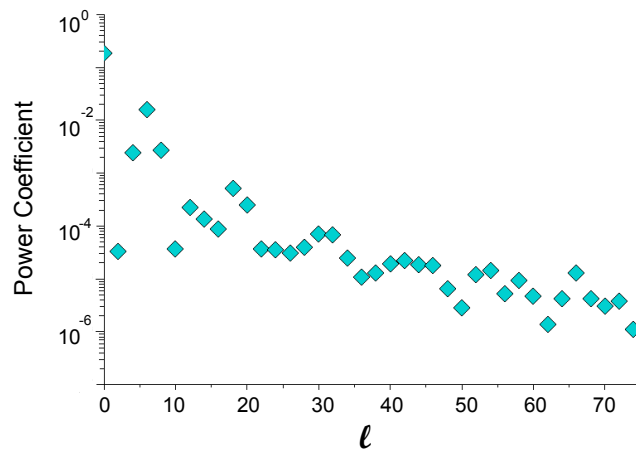


Figure 3.6: Power spectrum of the norm squared of  $\gamma_{l,m}$

ous grains is reduced. In the case depicted in Figure 3.7, each unit cell vector is reduced to a length of 2.61, indicating an approximately 8% shortening in each direction. Such a shortening leads to a denser packing of the unit cell. The volume of the cell depicted in Figure 3.7 is 17.78, about 21% smaller than a unit cell produced by touching spheres, whose volume is 22.43, while the volume of each grain is about 4.19, the volume of a unit sphere. Since the volumes of the grains remain nearly unchanged, flattening at intergranular contacts reduces the available interstitial space. The volume fraction of melt, assuming the void space is completely saturated with melt, is 0.05, substantially smaller than the interstitial melt volume fraction of 0.26 in the reference unit cell.

Both the melt volume fraction and contiguity varied with a variation in  $\epsilon$ . Figure 3.8 illustrates the relationships between  $\epsilon$  and melt volume fraction and contiguity. Melt volume fraction varies nearly linearly with  $\epsilon$ , while contiguity varies with  $\epsilon$  in a nonlinear manner.

The surface area and volume of the grain are measured for the different values of  $\epsilon$ . We found that the surface area and volume vary little from that of the unit sphere, which is used in the calculation of contiguity and melt volume fraction. The uncertainties in our data from these measurements are reported in the data table in Appendix C.

To fit our contiguity data and melt fraction data to a function, we used the MATLAB Curve Fitting Toolbox. We chose a 5<sup>th</sup> order polynomial of the form

$$\psi = p_1\phi^5 + p_2\phi^4 + p_3\phi^3 + p_4\phi^2 + p_5\phi + p_6, \quad (3.1)$$

to fit the data. To ensure that contiguity tends to unity at zero melt volume fraction, we fixed  $p_6 = 1$  in equation (3.1). The coefficients obtained from the

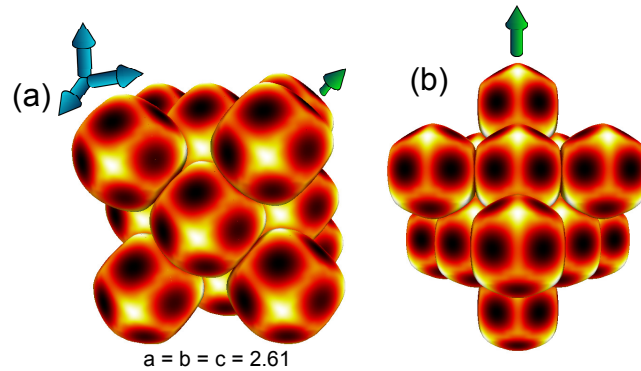


Figure 3.7: A calculated multiparticle unit cell with an FCC geometry. The dimension of each unit cell parameters  $a$ ,  $b$ , and  $c$  are equal to 2.61, approximately 8% shorter than an FCC packed with solid spheres, for which,  $a = b = c = 2.82$ . The volume of the unit cell is 17.72, while the volume of each grain is 4.19, leading to a melt volume fraction of 0.05. (a) The FCC unit cell with blue arrows indicating the edges of the cubic unit cell. The green arrow points in the direction of the normal to each close packed plane. (b) A view of the unit cell along the close packed planes.

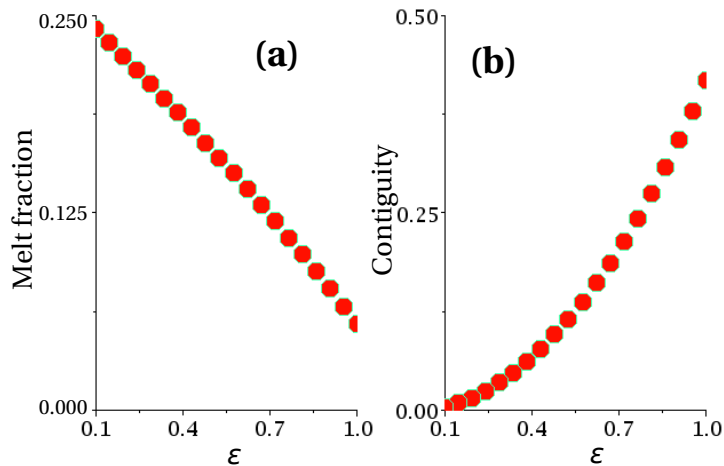


Figure 3.8: Plots showing the effect  $\epsilon$  has on (a) melt volume fraction and (b) contiguity. Increasing  $\epsilon$  results in greater grain-grain contact area and a denser packing arrangement. Notice how the relationship between  $\epsilon$  and melt volume fraction is nearly linear, while the relationship between  $\epsilon$  and contiguity is nonlinear.

$p_1$	$p_2$	$p_3$	$p_4$	$p_5$	$p_6$
-8065.00	6149.00	-1778.00	249.00	-19.77	1.00
-9844.00	5022.00	-2033.00	224.50	-20.59	0.00
-6287.00	7275.00	-1522.00	273.50	-18.94	0.00

Table 3.1: Parameters for fit to the contiguity ( $\psi$ ) as a function of melt fraction ( $\phi$ ). The fit is given by  $\psi = p_1\phi^5 + p_2\phi^4 + p_3\phi^3 + p_4\phi^2 + p_5\phi + p_6$ . The entries in the second and third row indicate the error bounds to the parameters within 95% confidence bound. For the fit the value of the sum of squared errors and  $R^2$  are  $1.67 \times 10^{-4}$  and 0.9995, respectively.

fitting function are given in Table 3.1. Measures for the goodness of the fit, sum of squared errors and  $R^2$  are given by  $1.67 \times 10^{-4}$  and 0.9995, respectively.

### 3.3 Comparison with previous studies

The results from this work are compared with the results from *von Bargen and Waff* (1986). The plot in Figure 3.9 compares our results and the fit to our data to the results from the model of *von Bargen and Waff* (1986) for a dihedral angle of  $\sim 30^\circ$ . Notice that the formula for solid-solid surface area in equation (8) of *von Bargen and Waff* (1986) needs to be corrected by adding a constant approximately equal to  $\pi$ , such that the plot of their equation (8) matches their Figure (7). In the article, their equation (8) erroneously indicates that the area of grain-grain contact decreases to zero at zero melt fractions. The results of *von Bargen and Waff* (1986) are only applicable for small melt fractions (less than 0.05 melt volume fraction) but the fit of the results are extrapolated with a dotted line for higher melt fractions in the plot.

In the same plot, our fit is extrapolated to zero melt fraction with a broken curve. As the curves indicate, between melt volume fractions of 0 and 0.02,

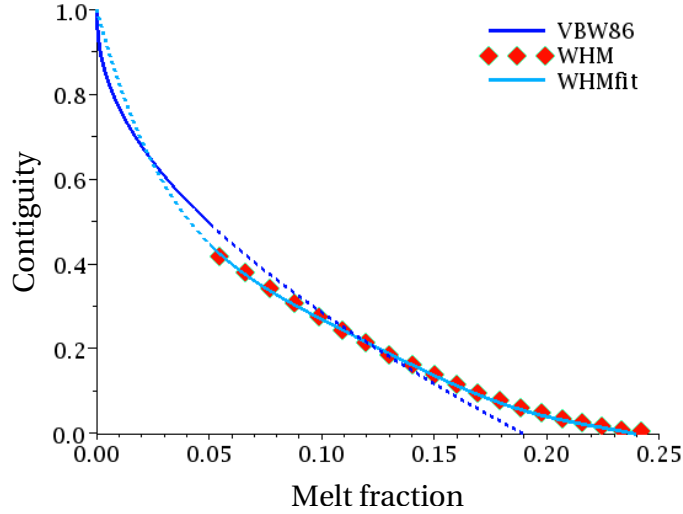


Figure 3.9: Comparison between contiguity from this work and the results of *von Bargen and Waff* (1986). The lines marked vBW86 and WHMfit corresponds to the model of *von Bargen and Waff* (1986) and the fit of our results, respectively. The results of *von Bargen and Waff* (1986) are limited to melt volume fractions below 0.05, but the fit is continued to higher melt fractions (dashed line). The red data points correspond to the results from this study.

our fit predicts a contiguity slightly lower than that of *von Bargen and Waff* (1986). Between melt volume fractions of 0.02 and 0.12, our model predicts a slightly higher value of contiguity than *von Bargen and Waff* (1986). The curves intersect at a melt volume fraction of 0.12 because of the flatness of our data with respect to that of *von Bargen and Waff* (1986) for the melt fractions investigated in this study. The curves intersect at a melt volume fraction of 0.02 because our contiguity is fixed at unity for a zero melt fraction, leading to a steeper curve for low melt fractions than the curve from *von Bargen and Waff* (1986). Finally, our model predicts that contiguity becomes zero at a disaggregation melt fraction of 0.26, while *von Bargen and Waff* (1986) predicts a disaggregation melt fraction of 0.19. Our slightly higher estimate of the disaggregation melt fraction agrees better with the results of *Scott and Kohlstedt* (2006), who report a rheological transition coincident with loss of contiguity,



that takes place between melt volume fractions of 0.25 and 0.3. Overall, the results from our model and that of *von Bargaen and Waff* (1986), are in good agreement. The similarity between these two models become clearer when compared with two dimensional models and measurements, discussed in the next section.

One source of variation between our work and *von Bargaen and Waff* (1986) arises from the different packing symmetry between the two models. The work of *von Bargaen and Waff* (1986) assumes tetrakaidecahedral geometry with a coordination number of 14 for each grain. As discussed before, our unit cell assumes rhombic dodecahedral geometry with a coordination number of 12. This study also investigated higher volume fractions while *von Bargaen and Waff* (1986) looked only at low melt volume fractions.

# Chapter 4

## Discussion

The result from this work bears a number of implications for the broader field of geophysics. First, our results demonstrate that contiguity measurements from three dimensional structures are different from those obtained from two dimensional sections. Second, using our contiguity-melt fraction data, we demonstrate that the seismic signature of the ULVZ at the core-mantle boundary can be explained by a smaller extent of melting than a two dimensional microstructure would predict. These topics are discussed in the following subsections.

## 4.1 Comparison with experimental data

The results from this work are compared with experimental measurements of contiguity. The plot in Figure 4.1 compares the results of our three dimensional study to the measurements of *Yoshino et al. (2005)*. *Yoshino et al. (2005)* compiled a large database consisting of measurements of contiguity from various partially molten aggregates. In this database, the authors reported contiguity measurements from synthetic mid-oceanic ridge basalt (MORB) and olivine bearing aggregate and a fertile spinel lherzolite rock from Killbourne Hole, New Mexico. Also plotted in Figure 4.1 are the results of the two dimensional study of *Hier-Majumder et al. (2006)*, and the results from the model of *von Bagen and Waff (1986)*.

Both the results of this study and that from *von Bagen and Waff (1986)* predict lower contiguity values than the two dimensional study of *Hier-Majumder et al. (2006)* and experimental measurements of *Yoshino et al. (2005)*, as depicted in Figure 4.1. The contrast increases at higher melt fractions. This shows that two dimensional studies may be limited at predicting contiguity for a given melt volume fraction, especially at higher melt fractions.

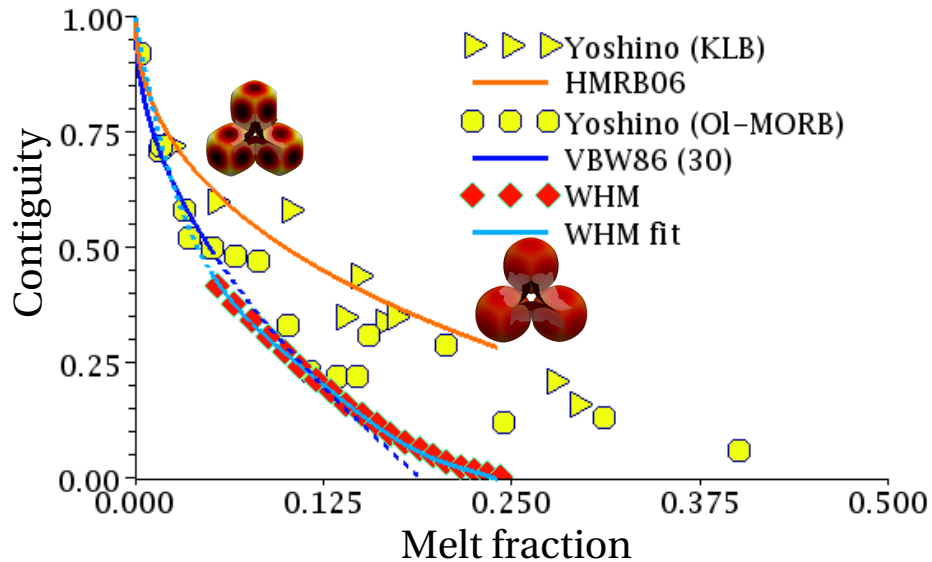


Figure 4.1: Comparison between contiguity from this work, the results of *von Bargen and Waff* (1986), the experimental measurements of *Yoshino et al.* (2005), and the two dimensional model of *Hier-Majumder et al.* (2006). The results of *von Bargen and Waff* (1986) are limited to melt volume fractions below 0.05, but the fit is continued to higher melt fractions (dashed line). Extrapolation of the fit to our data is also plotted as a broken line. The circular data points and the triangular data points indicate measurements by *Yoshino et al.* (2005) of Olivine-MORB and KLB, respectively. The orange and blue curves represent the contiguity-melt fraction relationships determined by the study of *Hier-Majumder et al.* (2006) and *von Bargen and Waff* (1986), respectively. The red data points are results found in this study. The plot shows that two dimensional models, and experimental measurements dependent on two dimensional slices, result in higher values of contiguity than three dimensional models.

The discrepancy between the experimental results and three dimensional numerical models can arise from two likely sources. First, the synthetic and natural partially molten rocks exhibit a variation in grain size, while all grains in our unit cell are identical. As the surface to volume ratio of grains change with their diameters, variation in grain size can cause some difference between the two data sets. The second factor arises simply from the fact that two dimensional sections can underestimate the melt volume fraction. *Hier-Majumder and Abbott* (2010) demonstrate that for a cubic grain with cylindrical tubules along edges, a two dimensional cross section underestimates the volume fraction of melt by a factor of 3. As a result, when the two dimensional data from their model was corrected to three dimensions, the contiguity decreased. Such correction were not applied to the two dimensional geometric model of *Hier-Majumder and Abbott* (2010) or the experimental measurements of *Yoshino et al.* (2005, Section 2.3).

## 4.2 Seismic properties

The value of contiguity at a given melt volume fraction is crucial in determining the physical properties of the rock. A large value of contiguity indicates a high fraction of grain-grain contact, which establishes a stronger skeletal network than for a partially molten rock with a lower contiguity. This indicates that the contiguity of the system, along with the melt volume fraction, strongly influences the effective elastic moduli of the system. Figure 4.2 shows the variation of the normalized shear and bulk modulus and the drop of seismic velocity of the partially molten rock as a function of melt volume fraction and contiguity. As expected, only the normalized shear modulus displays significant variation. The response of the bulk modulus to melting, in general,

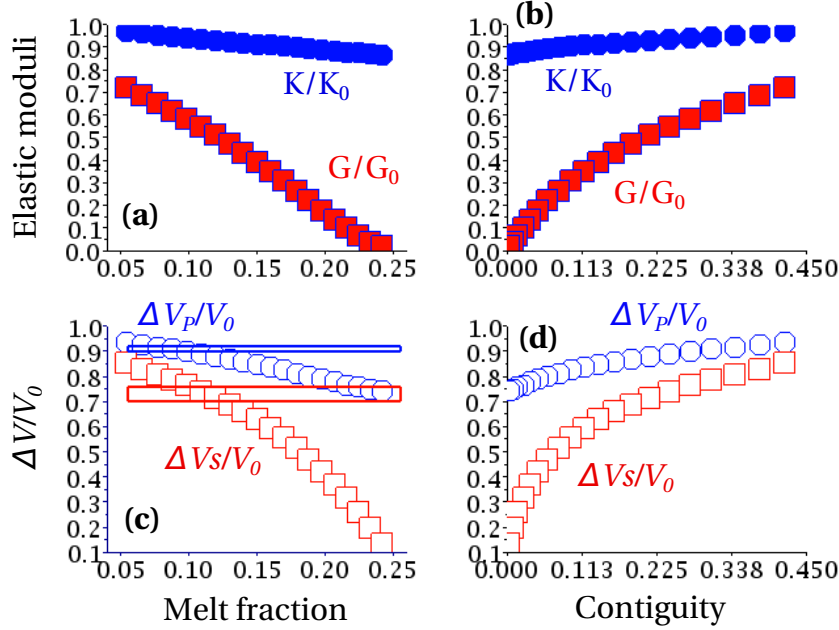


Figure 4.2: Plots of the changes in normalized shear and bulk modulus and the drop of seismic velocity of the partially molten rock as a function of melt volume fraction and contiguity. Plots (a) and (b) give the ratio between the effective bulk ( $K_{eff}$ ) and shear ( $N$ ) moduli and solid bulk ( $K$ ) and shear ( $\mu$ ) moduli in a partially molten aggregate as a function of melt volume fraction and contiguity, respectively. Plots (c) and (d) give the ratio of seismic velocities of a partially molten rock to the seismic velocities in the absence of melting as a function of melt volume and contiguity, respectively. The red and blue boxes in plot (c) give the range of observed velocity drops at the UltraLow Velocity Zone.

and contiguity in specific, is caused by the more modest contrast between the bulk moduli of the solid and the melt compared to the contrast between their respective shear moduli. As the contiguity decreases, grain surfaces become more wet and the strength of the skeletal framework decreases. This results in lower values of the shear modulus.

Figure 4.2 also shows the variation of normalized shear and  $P$  wave velocities as a function of melt volume fraction and contiguity. From the plot it can be seen that the shear wave velocity is much more sensitive to changes in contiguity and melt volume fraction than are  $P$  waves. When increasing

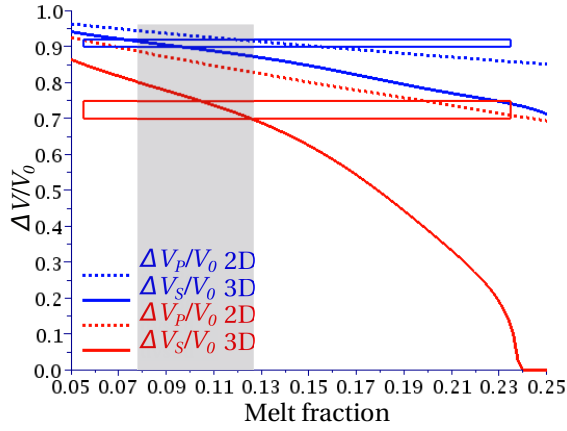


Figure 4.3: Ratio of seismic velocities of a partially molten rock to the seismic velocities in the absence of melting as a function of melt volume fraction. The seismic velocities from this study (solid lines) are compared to seismic velocities predicted by the two dimensional study of *Hier-Majumder et al.* (2006) (dotted lines). The horizontal red and blue boxes indicate the range of observed velocity drops at the Ultra-Low Velocity Zone. The vertical, shaded box is our predicted range of melt volume fraction, necessary to explain the observed seismic signature.

melt fraction from 0.10 to 0.20, the normalized shear wave velocity displays a reduction between 0.75 and 0.40, while the normalized  $P$  wave velocity experience a reduction between 0.90 and 0.80. For high values of melt fraction, the contiguity goes to near zero and shear wave velocity drops to zero, as expected. The drop in seismic velocities, and the ratio of  $P$  and shear wave velocity drop, provides a distinct seismic signature which will help constrain melting in the Earth's interior.

Our three dimensional model predicts a sharper reduction in shear and  $P$  wave velocities compared to the two dimensional, geometric model of *Hier-Majumder et al.* (2006). The plots in Figure 4.3 compares the seismic velocity reduction between these two cases. As the intersection between the horizontal boxes and the solid curves indicate, the observed shear and  $P$  wave velocity reductions between 0.70 to 0.75 and 0.90 to 0.92 can be explained by a range

of melt volume fractions between 0.08 and 0.12 using the three dimensional model. The two-dimensional model of *Hier-Majumder et al.* (2006) predicts similar velocity drops for much larger melt volume fractions. For example, a melt volume fraction as high as 0.23 can be used to explain the observed shear wave velocity reduction. As discussed earlier, the discrepancy between the two estimates arises from the overestimation of contiguity from two-dimensional models.

### 4.3 Implications for ULVZ

As discussed in section 1.1, Earth's core-mantle boundary is characterized by a patchwork of thin, dense ULVZ. Estimates for the extent of melting in these regions vary widely. Initial investigation of the seismic signal of this region was explained by *Williams and Garnero* (1996). Using a model of cylindrical melt inclusion along grain edges, they estimated a melt volume fraction of 0.3 was necessary to explain the nearly 30% drop in shear wave velocity and 10% drop in  $P$  wave velocity. One problem with this interpretation arises from the work of *Scott and Kohlstedt* (2006), who demonstrate that the partially molten aggregate becomes disaggregated at melt fractions of 0.25. At such high melt fractions, grain surfaces are completely coated by melt, leading to zero contiguity, as predicted by this model. Consequently, the inherent assumption regarding melt tubules along grain edges becomes physically untenable at such high melt fractions.

More recent estimates based on microstructural models of contiguity lead to the conclusion that a more modest amount of melt fraction, between 0.10 and 0.15 likely causes the observed seismic signature (*Hier-Majumder*, 2008). The plot of seismic velocity reduction based on the current work indicates that up to



20% reduction of shear wave velocity can be obtained at a melt volume fraction of 0.08, consistent with the recent estimates. One important consequence of melting far below the disaggregation melt fraction involves the viscosity of the ULVZ. *Scott and Kohlstedt* (2006) indicate that the viscosity of a partially molten aggregate is reduced by melting following the relation  $\eta/\eta_0 = \exp -\alpha\phi$ , where  $\eta$  is the viscosity of the partially, molten rock,  $\eta_0$  is the viscosity of the solid,  $\phi$  is the melt volume fraction, and  $\alpha$  is a dihedral angle dependent coefficient which assumes the value of 25 for an olivine-MORB aggregate. If the seismic signature of the ULVZ is explained by the relatively modest amount of melting, the viscosity of this region is reduced by approximately one to two orders of magnitude. Laboratory experiments on the stability of plumes (*Jellinek and Manga*, 2004) and a gravity current model of ULVZ spreading (*Hier-Majumder and Revenaugh*, 2009) predict that the ULVZ is likely two orders of magnitude weaker than the ambient mantle. The large degree of melting predicted by the two dimensional model of contiguity, however, will reduce the effective viscosity to values much lower than these estimates.

# Chapter 5

## Conclusion

The model described here provides a new three dimensional, microgeodynamic model of contiguity in partially molten rocks. This model incorporates aspects of both geometric models and dynamic models to fully describe how the microstructure behaves. In our model, the FCC unit cell contains 14 rhombic dodecahedral grains. Our results extend the range of available contiguity-melt fraction model from a melt fraction of 0.05 to the disaggregation fraction of 0.26.

The values of contiguity are found to agree well with the model of *von Bargen and Waff* (1986), when extrapolating the studies to fit the appropriate range of melt fractions. Our results predict lower values of contiguity than the experimental results of *Yoshino et al.* (2005) and the two dimensional study of *Hier-Majumder et al.* (2006), for a given melt volume fraction. Consequently, the three dimensional model predicts a larger drop in seismic velocities for a given melt fraction than two dimensional models. When applied to the Earth's core mantle boundary, if the solid phase has properties similar to that predicted by the PREM model, the observed ULVZ can be explained by a melt volume fraction between 0.08 and 0.12.

# Appendix A

## Analytical solution for the flow field

-

This thesis employs the method of vector solid harmonics to obtain analytical solutions for the velocity and pressure fields within each grain and the melt phase. A detailed description of this method is given by (Leal, 1992, Ch. 4). This technique is useful to construct solutions from a characteristic vector or tensorial quantity. First, we notice that the velocity of the melt phase,  $\mathbf{u}_m$  can be expressed as a function of dynamic pressure  $P_m$  and a yet to be determined harmonic function  $\mathbf{v}_m$  ( $\nabla^2 \mathbf{v}_m = 0$ ) as

$$\mathbf{u}_m = \frac{1}{2} \mathbf{x} P_m + \mathbf{v}_m, \quad (\text{A.1})$$

where  $\mathbf{x}$  is the position vector. Such a prescription of velocity guarantees that the momentum conservation equation, (2.6), is automatically satisfied. Next, we substitute this velocity into the equation for mass conservation, (2.7), to obtain an additional constraint on the harmonic function  $\mathbf{v}_m$ ,

$$\nabla \cdot \mathbf{v}_m = -\frac{1}{2} (\mathbf{x} \cdot \nabla P_m + 3P_m). \quad (\text{A.2})$$

With the decomposition of the velocity field, given by equation (A.1) and the additional constraint (A.2), the solutions automatically satisfy the mass and momentum conservation equations. The next step is to build the harmonic function  $\mathbf{v}_m$  from a characteristic vector  $\mathbf{d}$  relevant to the system. This vector should be constant, but, as we demonstrate, this vector does not appear in the steady state equation for shape function. The vector  $\mathbf{d}$  needs to be constant over the length scales and time scales of the sintering process. One possible choice of this vector can be the displacement vector between the centers of two particles. Finally, two additional constraints must be observed while building the solutions. Since the origin is fixed within the center of the grain, the flow

fields within the grains must be well behaved at the origin. Similarly, the solutions for the melt phase must tend to zero at infinite distance as the melt phase is considered surrounding the solid grain. The standard procedure in drop dynamics is to build the solution vector within the grain using growing harmonics (only positive powers of  $r$ , the distance from the center); while using decaying harmonics (negative powers of  $r$ ) to build the solution outside the grain. With these considerations in mind, we select the test solution for the harmonic function  $\mathbf{v}_m$  as

$$\mathbf{v}_m = \alpha_1 \left( \frac{\mathbf{x}(\mathbf{d} \cdot \mathbf{x})}{r^5} - \frac{\mathbf{d}}{3r^3} \right) + \beta_1 \frac{\mathbf{d}}{r} \quad (\text{A.3})$$

where  $\alpha_1$  and  $\beta_1$  are constant coefficients that are yet to be determined. Next, we notice that the pressure field within a constant viscosity fluid is always a scalar harmonic function (*Leal, 1992*). Thus, we select the trial function for the pressure field inside the melt,  $P_m$ , as

$$P_m = c_1 \frac{\mathbf{x} \cdot \mathbf{d}}{r^3} \quad (\text{A.4})$$

Similarly, we build the trial solutions for pressure and the harmonic component of velocity within the grain, subscript  $g$ , as

$$P_g = c_2 \mathbf{d} \cdot \mathbf{x}, \quad (\text{A.5})$$

and,

$$\mathbf{v}_g = \alpha_2 (\mathbf{x}(\mathbf{d} \cdot \mathbf{x}) - r^2 \mathbf{d}), \quad (\text{A.6})$$

where  $c_2$  and  $\alpha_2$  are constants that are yet to be determined.

Next, we proceed to evaluate the four unknown constants. First, we sub-

stitute the trial solutions for melt pressure  $P_m$  and the harmonic component  $\mathbf{v}_m$  into equation (A.2) to yield, the relation,

$$\beta_1 = \frac{c_1}{2}. \quad (\text{A.7})$$

Equation (A.7) is obtained by observing,

$$\mathbf{x} \cdot \nabla P_m = -2c_1 \frac{\mathbf{d} \cdot \mathbf{x}}{r^3} \quad (\text{A.8})$$

which can be rewritten as

$$3P_m + \mathbf{x} \cdot \nabla P_m = c_1 \frac{\mathbf{d} \cdot \mathbf{x}}{r^3} \quad (\text{A.9})$$

and can be combined with (A.2) and

$$\nabla \cdot \mathbf{v}_m = -\beta_1 \frac{\mathbf{d} \cdot \mathbf{x}}{r^3} \quad (\text{A.10})$$

to yield equation (A.7). From (A.1), (A.4), (A.3), and (A.7), the velocity profile for the melt simplifies to

$$\mathbf{u}_m = \left( \frac{c_1}{2r^3} + \frac{\alpha_1}{r^5} \right) \mathbf{x}(\mathbf{d} \cdot \mathbf{x}) + \left( \frac{c_1}{2r} - \frac{\alpha_1}{3r^3} \right) \mathbf{d} \quad (\text{A.11})$$

In a similar manner, we can establish a relationship between  $c_2$  and  $\alpha_2$  by noticing

$$3P_g + \mathbf{x} \cdot \nabla P_g = 4c_2 \mathbf{d} \cdot \mathbf{x}, \quad (\text{A.12})$$

and

$$\nabla \cdot \mathbf{v}_g = 2\alpha_2 \mathbf{d} \cdot \mathbf{x}. \quad (\text{A.13})$$

Similar to the constraint on  $\mathbf{v}_m$  provided, by equation (A.2), we can also write,

$$\nabla \cdot \mathbf{v}_g = -\frac{1}{2}(3P_g + \mathbf{x} \cdot \nabla P_g). \quad (\text{A.14})$$

Substituting the terms from equations (A.12) and (A.13) into equation (A.14), we arrive at,

$$\alpha_2 = -c_2. \quad (\text{A.15})$$

This simplifies (A.6) to

$$\mathbf{u}_m = \alpha_2 \left( \frac{1}{2} \mathbf{x} (\mathbf{d} \cdot \mathbf{x}) - r^2 \mathbf{d} \right) \quad (\text{A.16})$$

We use mass conservation equation for both phases, the normal, and tangential components of the no-slip boundary condition to obtain the relations,

$$\alpha_1 = \frac{9\alpha_2}{8}, \quad (\text{A.17})$$

$$\beta_1 = -\frac{5\alpha_2}{8}, \quad (\text{A.18})$$

$$c_1 = -\frac{5\alpha_2}{4}, \quad (\text{A.19})$$

$$c_2 = -\alpha_2. \quad (\text{A.20})$$

We plug in the solutions for the velocity and pressures at  $r = 1$  into the normal component of the stress jump boundary condition, equation (2.9), which, after some algebra, yields,

$$\left( \frac{3}{4} + \lambda \right) \alpha_2 \mathbf{d} \cdot \mathbf{x} = \frac{2\gamma_1 - \gamma_0 \nabla^2 f}{Ca} \quad (\text{A.21})$$



which can be simplified to

$$\mathbf{d} \cdot \mathbf{x} = \frac{8\gamma_1 - 4\gamma_0 \nabla^2 f}{\alpha_2 Ca(3 + 4\lambda)} \quad (\text{A.22})$$

where  $Ca$  is given by equation (2.18).

The kinematic condition (2.12) is simplified to

$$\frac{\partial f}{\partial t} = \mathbf{u}_m \cdot \mathbf{x} \quad (\text{A.23})$$

which is solved using (A.16)

$$\frac{\partial f}{\partial t} = -\frac{\alpha_2}{2} \mathbf{d} \cdot \mathbf{x} \quad (\text{A.24})$$

Combining equation (A.22) and (A.24), and eliminating  $\mathbf{d} \cdot \mathbf{x}$  and  $\alpha_2$  gives equation (2.17).

# Appendix B

## Prescription of contact faces

Grain-grain contact patches are prescribed using step functions in  $\theta$  and  $\phi$ . To build rhombus shaped contact faces, multiple rectangular patches are built using step functions for each face. For the equatorial contact faces, 5 rectangular patches in  $\theta$ - $\phi$  are needed, while only 4 are needed for the contact faces above and below the equatorial contacts, see Figure 2.3. The shortening of the strips in  $\phi$  was necessary to prevent overlapping of the contact faces near poles.

To control the size of these contact faces, five parameters were introduced:  $wt$ ,  $wp$ ,  $wtpole$ ,  $wte$ , and  $wpe$ , see Figure B.1. The parameters  $wt$  and  $wp$  shift the contact faces above and below the equator away from the neighboring contact faces in the  $\theta$  and  $\phi$  direction, respectively. Increasing the parameter  $wtpole$  shifts the same contact faces away from the pole. The parameters  $wte$  and  $wpe$  shift the contact faces along the equator away from the neighboring contact faces in the  $\theta$  and  $\phi$  direction, respectively. The lengths of these parameters are measured from the center of the corresponding melt channel, so that increased values of these parameters produce smaller contact faces. This means that the distance between two contact faces is 2 times that of the  $w$  parameter, excluding  $wtpole$ . In this study the following parameters were used:  $wt = 0.11$ ,  $wp = 0.17$ ,  $wtpole = 0.03$ ,  $wte = -0.02$ ,  $wpe = 0.09$ .

For smaller contact faces, rectangular patches may be used. The size and shape of these rectangular patches are controlled by four parameters:  $stp$ ,  $spp$ ,  $ste$ , and  $spe$ , see Figure B.1. The rectangular patches take the size and shape given by these parameter when they are within the rhombus shape provided by the  $w$  parameters. For larger areas of contact, the rectangular patches increase in size until they reach the edge of the rhombus, corresponding to the face of a rhombic dodecahedron, see (*Lissant*, 1966, Figure 2). Thus for large values

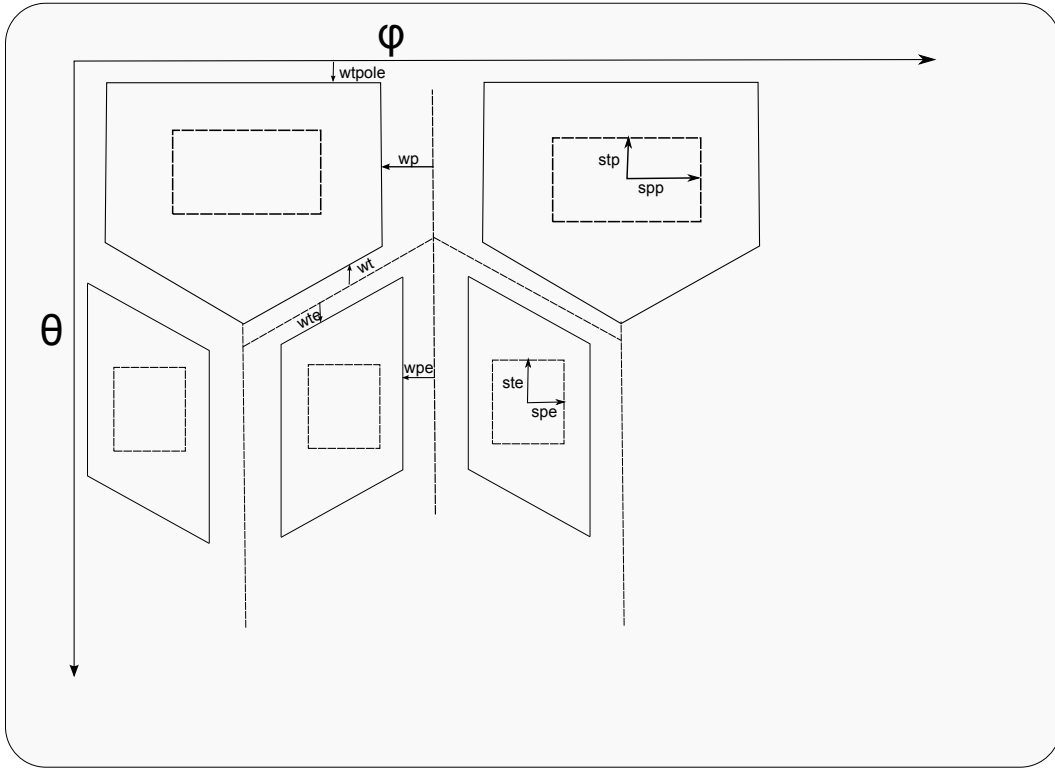


Figure B.1: Parameters used to prescribe the size and shape of contact patches.

of  $stp$ ,  $spp$ ,  $ste$ , and  $spe$  the shape of the contact patch will be a rhombus. It was found that smaller contact faces did not significantly affect the contiguity of the system. Because of this we used the full rhombus shape described by the  $w$  parameters, and varied the contiguity using  $\epsilon$ .

# Appendix C

## Data table

Table C.1: Contiguity and melt fraction measurements

$\epsilon$	Melt Volume %	Contiguity
1.000	$5.45 \pm 0.27$ %	$0.418 \pm 0.009$
0.953	$6.58 \pm 0.24$ %	$0.379 \pm 0.007$
0.905	$7.69 \pm 0.21$ %	$0.342 \pm 0.006$
0.858	$8.79 \pm 0.18$ %	$0.307 \pm 0.005$
0.811	$9.86 \pm 0.16$ %	$0.274 \pm 0.004$
0.763	$10.92 \pm 0.13$ %	$0.243 \pm 0.003$
0.716	$11.97 \pm 0.11$ %	$0.214 \pm 0.002$
0.668	$12.99 \pm 0.09$ %	$0.187 \pm 0.002$
0.621	$14.01 \pm 0.07$ %	$0.161 \pm 0.001$
0.574	$15.01 \pm 0.06$ %	$0.137 \pm 0.001$

Table C.1: continued...

---

$\epsilon$	Melt Volume %	Contiguity
0.526	$15.99 \pm 0.04$ %	$0.116 \pm 0.001$
0.479	$16.95 \pm 0.03$ %	$0.096 \pm 0.001$
0.432	$17.91 \pm 0.02$ %	$0.078 \pm 0.000$
0.384	$18.84 \pm 0.01$ %	$0.062 \pm 0.000$
0.337	$19.77 \pm 0.00$ %	$0.047 \pm 0.000$
0.289	$20.68 \pm 0.18$ %	$0.035 \pm 0.000$
0.242	$21.57 \pm 0.02$ %	$0.024 \pm 0.000$
0.195	$22.46 \pm 0.02$ %	$0.016 \pm 0.000$
0.147	$23.33 \pm 0.03$ %	$0.009 \pm 0.000$
0.100	$24.18 \pm 0.03$ %	$0.004 \pm 0.000$

---

# Bibliography

- Bercovici, D., and S. Karato, Whole-mantle convection and the transition zone water filter, *Nature*, *425*, 39–44, 2003.
- Berryman, J., Long-wavelength propagation in composite elastic media, 1, spherical inclusions, *J. Acoust. Soc. Am.*, *68*, 1809–1819, 1980a.
- Berryman, J., Long-wavelength propagation in composite elastic media, 2, ellipsoidal inclusions, *J. Acoust. Soc. Am.*, *68*, 1820–1831, 1980b.
- Courtier, A. M., and J. Revenaugh, Deep upper-mantle melting beneath the tasman and coral seas detected with multiple scs reverberations, *Earth and Planetary Science Letters*, *259*, 66–76, 2007.
- Daines, M. J., and D. L. Kohlstedt, Influence of deformation in melt topology in peridotites, *Journal of Geophysical Research*, *102*(B5), 10,257– 10,271, 1997.
- Dasgupta, R., and M. M. Hirschmann, Melting in the earth’s deep upper mantle caused by carbon dioxide, *Nature*, *440*, 659–662, doi:10.1038/nature04612, 2006.
- Dasgupta, R., and M. M. Hirschmann, The deep carbon cycle and melting in Earth’s interior, *Earth Planet Sci. Lett*, *298*, 1–13, doi: 10.1016/j.epsl.2010.06.039, 2010.
- Faul, U. H., Melt retention and segregation beneath midocean ridges, *Nature*, *410*, 920–923, 2001.
- Fischer, K. M., H. A. Ford, D. L. Abt, and C. A. Rychert, The Lithosphere-Asthenosphere Boundary, in *ANNUAL REVIEW OF EARTH AND PLANETARY SCIENCES, VOL 38, Annual Review of Earth and Planetary Sciences*, vol. 38, pp. 551–575, doi:10.1146/annurev-earth-040809-152438, 2010.
- Garnero, E., and A. K. McNamara, Structure and dynamics of Earth’s lower mantle, *Science*, *320*, 626–628, 2008.
- German, R., *Liquid Phase Sintering*, Plenum Press, 1985.



- Hernlund, J. W., and A. M. Jellinek, Dynamics and structure of a stirred partially molten ultralow-velocity zone, *Earth and Planetary Science Letters*, 296(1-2), 1 – 8, doi:10.1016/j.epsl.2010.04.027, 2010.
- Hernlund, J. W., and P. J. Tackley, Some dynamical consequences of partial melting in earth’s deep mantle, *Physics of the Earth and Planetary Interiors*, 162, 149–163, 2007.
- Hier-Majumder, S., Influence of contiguity on seismic velocities of partially molten aggregates, *Journal of Geophysical Research*, 113, B12,205, doi:10.1029/2008JB005662, 2008.
- Hier-Majumder, S., Development of anisotropic mobility during two-phase flow, *Geophysical Journal International*, 185, doi:doi: 10.1111/j.1365-246X.2011.05024.x, 2011.
- Hier-Majumder, S., and M. E. Abbott, The influence of dihedral angle on seismic velocities of partially molten rocks., *Earth Planet. Sci. Lett.*, 299, 23–32, doi:10.1016/j.epsl.2010.08.007, 2010.
- Hier-Majumder, S., and J. Revenaugh, Relationship between the viscosity and the topography of the ultralow-velocity zone near the core-mantle boundary, *Submitted to Earth and Planetary Science Letters*, 2009.
- Hier-Majumder, S., P. H. Leo, and D. L. Kohlstedt, On grain boundary wetting during deformation, *Acta Materialia*, 52(12), 3425–3433, doi:10.1016/j.actamat.2004.03.040, 2004.
- Hier-Majumder, S., Y. Ricard, and D. Bercovici, Role of grain boundaries in magma migration and storage, *Earth and Planetary Science Letters*, 248, 735–749, doi:10.1016/j.epsl.2006.06.015, 2006.
- Hirschmann, M. M., Partial melt in the oceanic low velocity zone, *PHYSICS OF THE EARTH AND PLANETARY INTERIORS*, 179(1-2), 60–71, doi: 10.1016/j.pepi.2009.12.003, 2010.
- Holtzman, B. K., D. L. Kohlstedt, M. E. Zimmerman, F. Heidelbach, T. Hiraga, and J. Hustoft, Melt segregation and strain partitioning: Implications for seismic anisotropy and mantle flow, *Science*, 301, 1227–1230, 2003.
- Hopper, R., Plane stokes flow driven by capillarity on a free surface, *Journal of Fluid Mechanics*, 213, 349–375, 1990.
- Hopper, R., Coalescence of two viscous cylinders by capillarity: Part I, Theory, *Journal of the American Ceramics Society*, 76, 2947–2952, 1993a.
- Hopper, R., Coalescence of two viscous cylinders by capillarity: Part II, Shape evolution, *Journal of the American Ceramics Society*, 76, 2953–2960, 1993b.

- Hustoft, J., and D. Kohlstedt, Metal silicate segregation in deforming dunitic rocks, *Geochemistry Geophysics Geosystems*, 7(Q02001), 2006.
- Hutko, A., T. Lay, and J. Revenaugh, Localized double-array stacking analysis of pcp: D'' and ulvz structure beneath the cocos plate, mexico, central pacific and north pacific, *Phys. Earth Planet. Int.*, 173, 60–74, 2009.
- Jansons, K., Moving contact lines on a two-dimensional rough surface, *Journal of Fluid Mechanics*, 154, 1–28, 1984.
- Jellinek, A., and M. Manga, Links between long-lived hotspots, mantle plumes D'', and plate tectonics, *Reviews of Geophysics*, 42(RG3002), 2004.
- Jurewicz, S. R., and E. Watson, The distribution of partial melt in a granitic system: The application of liquid phase sintering theory, *Geochimica et Cosmochimica Acta*, 49(5), 1109 – 1121, doi:10.1016/0016-7037(85)90002-X, 1985.
- Kang, S.-j. L., *Sintering: Densification, Grain Growth and Microstructure*, Elsevier, 2005.
- Katz, R. F., M. Spiegelman, and B. Holtzman, The dynamics of melt and shear localization in partially molten aggregates., *Nature*, 442, 676–679, 2006.
- Kawakatsu, H., P. Kumar, Y. Takei, M. Shinohara, T. Kanazawa, E. Araki, and K. Suyehiro, Seismic Evidence for Sharp Lithosphere-Asthenosphere Boundaries of Oceanic Plates, *SCIENCE*, 324(5926), 499–502, doi: 10.1126/science.1169499, 2009.
- Kingery, W., Densification during sintering in the presence of a liquid phase. I: Theory, *Journal of Applied Physics*, 30(3), 301–306, 1959.
- Kuiken, H., Viscous sintering: The surface-tension-driven flow of a liquid form under the influence of curvature gradient at its surface, *Journal of Fluid Mechanics*, 214, 503–515, 1993.
- Leal, G., *Laminar Flow and Convective Transport Processes*, Butterworth-Heinemann, 1992.
- Lissant, K. J., The geometry of high-internal-phase-ratio emulsions, *Journal of Colloid and Interface Science*, 22, 462–468, 1966.
- Manga, M., and H. Stone, Low reynolds number motion of bubbles, drops, and rigid spheres through fluid-fluid interfaces, *Journal of Fluid Mechanics*, 287, 279–298, 1995.
- Mao, W. L., H.-K. Mao, W. Sturhahn, J. Zhao, V. B. Prakapenka, Y. Meng, J. Shu, Y. Fei, and R. J. Hemley, Iron-rich post perovskite and the origin of the ultra low velocity zone, *Science*, 312, 564–565, 2006.

- Mavko, G., Velocity and attenuation in partially molten rocks, *J. Geophys. Res.*, *80*, 5173–5189, 1980.
- McNamara, A. K., E. J. Garnero, and S. Rost, Tracking deep mantle reservoirs with ultra-low velocity zones, *Earth and Planetary Science Letters*, *299*(1-2), 1–9, 2010.
- Mosenfelder, J. L., P. D. Asimow, and T. J. Ahrens, Thermodynamic properties of  $\text{Mg}_2\text{SiO}_4$  liquid at ultra-high pressures from shock measurements to 200 Gpa on forsterite and wadsleyite, *Journal of Geophysical Research, B, Solid Earth and Planets*, *112*(B06208), 2007.
- Nomura, R., H. Ozawa, S. Tateno, K. Hirose, J. Hernlund, S. Muto, H. Ishii, and N. Hiraoka, Spin crossover and iron-rich silicate melt in the earth’s deep mantle, *Nature*, *473*, 199 – 202, doi:10.1038/nature09940, 2011.
- O’Connell, R., and B. Budiansky, Seismic velocities in drt and saturated cracked solids, *J. Geophys. Res.*, *79*, 5412–5426, 1974.
- Ozawa, H., K. Hirose, M. Mitome, Y. Bando, N. Sata, and Y. Ohishi, Chemical equilibrium between ferropericlase and molten iron to 134 GPa and implications for iron content at the bottom of the mantle, *Geophys. Res. Lett.*, *35*(L05308), doi:10.1029/2007GL032648, 2008.
- Ozawa, H., K. Hirose, M. Mitome, Y. Bando, N. Sata, and Y. Ohishi, Experimental study of reaction between perovskite and molten iron to 146 GPa and implications for chemically distinct buoyant layer at the top of the core, *Phys Chem Minerals*, *36*, 355–363, 2009.
- Park, H. H., and D. K. Yoon, Effect of dihedral angle on the morphology of grains in a matrix phase, *Metallurgical Transactions, A*, *16 A*, 923–928, 1985.
- Press, W. H., S. A. Teukolsky, W. T. Vetterling, and B. P. Flannery, *Numerical recipes in FORTRAN*, chap. 19.6, 2 ed., Cambridge University Press, 1992.
- Revenaugh, J., and S. Sipkin, Seismic evidence for silicate melt atop the 410-km mantle discontinuity, *Nature*, *369*, 474–476, 1994.
- Rost, S., and J. Revenaugh, Small scale ultralow-velocity zone structure imaged by *ScP*, *Journal of Geophysical Research*, *108*(B12056), 2003.
- Rost, S., E. J. Garnero, Q. Williams, and M. M., Seismological constraints on a possible plume root at the core-mantle boundary, *Nature*, *435*, 666–669, 2005.

- Rychert, C. A., S. Rondenay, and K. M. Fischer, P-to-S and S-to-P imaging of a sharp lithosphere-asthenosphere boundary beneath eastern North America, *JOURNAL OF GEOPHYSICAL RESEARCH-SOLID EARTH*, 112(B8), doi:10.1029/2006JB004619, 2007.
- Scott, T., and D. Kohlstedt, The effect of large melt fraction on the deformation behavior of peridotite, *Earth and Planetary Science Letters*, 246(3-4), 177–187, 2006.
- Stixrude, L., and B. Karki, Structure and freezing of MgSiO<sub>3</sub> liquid in Earth's lower mantle, *Science*, 310,, 297–299, 2005.
- Takei, Y., Constitutive mechanical relations of solid-liquid composites in terms of grain boundary contiguity, *Journal of Geophysical Research*, 103, 18,183–18,203, 1998.
- Takei, Y., Acoustic properties of partially molten media studied on a simple binary system with a controllable dihedral angle, *Journal of Geophysical Research*, 105, 16,665–16,682, 2000.
- Takei, Y., Effect of pore geometry on  $v_p/v_s$ : From equilibrium geometry to crack, *Journal of Geophysical Research*, 107, 2043, 2002.
- Takei, Y., Deformation induced grain boundary wetting and its effect on acoustic and rheological properties of partially molten rock analogue, *Journal of Geophysical Research*, 110, B12,203, 2005.
- Tauzin, B., E. Debayle, and G. Wittlinger, Seismic evidence for a global low-velocity layer within the Earth's upper mantle, *Nature*, 3, 718–721, doi:10.1038/NGEO969, 2010.
- ten Grotenhuis, S., M. Drury, C. Spiers, and C. J. Peach, Melt distribution in olivine rocks based on electrical conductivity experiments, *Journal of Geophysical Research, B, Solid Earth and Planets*, 110(B12201), 2005.
- Vinnik, L., and V. Farra, Low s velocity atop the 410-km discontinuity and mantle plumes, *Earth Planet Sci. Lett.*, 262, 398–412, doi:10.1016/j.epsl.2007.07.051, 2007.
- von Bargen, N., and H. Waff, Permeabilities, interfacial areas and curvatures of partially molten systems: results of numerical computations of equilibrium microstructures, *Journal of Geophysical Research*, 91, 9261–9276, 1986.
- Wen, L., and D. Helmberger, Ultra-low velocity zones near the core-mantle boundary from broadband PKP precursors, *Science*, 279, 1701–1703, 1998.

- Wicks, J. K., J. M. Jackson, and W. Sturhahn, Very low sound velocities in iron-rich (Mg,Fe)O: Implications for the core-mantle boundary region, *Geophysical Research Letters*, *37*(15), 1–5, doi:10.1029/2010GL043689, 2010.
- Williams, Q., and E. Garnero, Seismic evidence for partial melt at the base of Earth's mantle, *Science*, *273*, 1528–1530, 1996.
- Wray, P. J., The geometry of two-phase aggregates in which the shape of the second phase is determined by its dihedral angle, *Acta Metall.*, *24*, 125–135, 1976.
- Yoshino, T., Y. Takei, D. Wark, and E. Watson, Grain boundary wetness of texturally equilibrated rocks, with implications for seismic properties of the upper mantle, *Journal of Geophysical Research*, *110*, B08,205, 2005.
- Zhu, W., G. A. Gaetani, F. Fuisseis, L. G. J. Montsi, and F. De Carlo, Microtomography of partially molten rocks: three-dimensional melt distribution in mantle peridotite, *Science*, *332*(6025), 88 – 91, doi:10.1126/science.1202221, 2011.
- Zimmerman, M. E., S. Zhang, D. L. Kohlstedt, and S.-I. Karato, Melt distribution in mantle rocks deformed in shear, *Geophysical Research Letters*, *26*(10), 1505–1508, 1999.